The odd-number cyclo[13]carbon and its dimer cyclo[26]carbon

Authors: Florian Albrecht,[1†] Igor Rončević,[2†] Yueze Gao[2†], Fabian Paschke[1†], Alberto Baiardi[3], Ivano Tavernelli[3], Shantanu Mishra[1], Harry L. Anderson[2]* and Leo Gross[1]*

Affiliations:

[1] IBM Research Europe – Zürich, 8803 Rüschlikon, Switzerland.

[2] Department of Chemistry, Oxford University, Chemistry Research Laboratory, Oxford, United Kingdom.

[3] IBM Quantum, IBM Research Europe – Zürich, 8803 Rüschlikon, Switzerland.

† These authors contributed equally.

*Corresponding authors. Email: harry.anderson@chem.ox.ac.uk; lgr@zurich.ibm.com

Abstract: Cyclo[*N*]carbons (C$_N$) are molecular rings of *N* carbon atoms. These exotic carbon allotropes are excellent benchmarking systems for testing quantum chemical theoretical methods, and they may be valuable precursors to other carbon-rich materials. Odd-*N* cyclocarbons, elusive to date, are predicted to be even less stable than even-*N* ones, and their structures are unknown. Here we report the on-surface synthesis of cyclo[13]carbon, C$_{13}$. We elucidate its properties by scanning probe microscopy and theoretical modelling. C$_{13}$ adopts an open-shell configuration with a triplet ground state and a kinked geometry, which shows different degrees of pronunciation related to different degrees of carbene localization. Moreover, we prepare and characterize the C$_{13}$ dimer, yielding cyclo[26]carbon, demonstrating the potential of cyclocarbons as precursors to novel carbon allotropes.

(max. 125 words)

One-Sentence Summary: The odd-number cyclo[13]carbon has a triplet ground state, a localized carbene center and can dimerize to cyclo[26]carbon.

(max 125 characters)

Main Text: Recently, the family of carbon allotropes was expanded by the generation and on-surface characterization of cyclo[N]carbons (C_N), molecular rings composed of N carbon atoms. Several even-N cyclocarbons have been structurally characterized ([1-4]). On the one side, cyclocarbons are relatively small and their electronic structure resembles that of a particle on a ring and can be rationalized with text-book physics ([5, 6]). On the other side, many energy-degenerate orbitals and multiple possible Jahn-Teller distortions render calculations extremely demanding ([7-13]), making cyclocarbons excellent model systems to benchmark theoretical approaches ([14]). For many years, cyclocarbons could experimentally only be studied in the gas phase ([15, 16]) or in a solid matrix ([17]). Only recently, even-N cyclocarbons with $N = 10, 12, 14, 16, 18, 20$ ([1-4]) have been generated by on-surface synthesis ([18]) using atom manipulation techniques and were characterized by non-contact atomic force microscopy (AFM) with CO functionalized tips ([19]) and scanning tunnelling microscopy (STM) on NaCl surfaces at low temperature.

Even-N cyclocarbons can be doubly aromatic, with $N = (4k + 2)$, where k is an integer, or doubly anti-aromatic with $N = 4k$. In agreement with recent theoretical predictions ([11]), the doubly aromatic ($4k + 2$) cyclocarbons show significant bond-angle alternation (BAA) and no measurable bond-length alternation (BLA) for $N < 14$ ([3]), but large BLA for $N > 14$ ([1, 20]) (see also C_{26}, characterized below, in this work). In this series, C_{14} is the transition structure, with small BLA and strong BAA ([3, 11]). The $4k$ cyclocarbons studied show strong BLA indicative of a doubly anti-aromatic ground state ([2, 4]). In general, even-N cyclocarbons exhibit $N/2$ symmetry, i.e., $C_{(N/2)h}$ or $D_{(N/2)h}$, a closed-shell singlet ground state, and the structural distortions to be considered are only BLA and BAA. In contrast, odd-N cyclocarbons cannot form $C_{(N/2)h}$ nor $D_{(N/2)h}$ geometries, but might adopt more symmetric, i.e., D_{Nh} or more distorted, e.g., C_s or C_{2v} shapes and are expected to be even less stable then even-N cyclocarbons ([9, 10]). In addition, an odd number of electrons in the π-systems increases the number of ground states that need to be considered, including open-shell and high-spin configurations ([12]). Moreover, localized carbene centers can occur as an additional element of distortion. Thus odd-N cyclocarbons are structurally highly complex and extremely challenging to predict ([12]).

Here, in conjunction with theoretical modeling, we report the experimental structural characterization of an odd-N cyclocarbon, i.e., C_{13}. Inspired by precursors used by W. Xu et al. ([3]), we prepared C_{13}, a cyclocarbon of the $N = (4k + 1)$ series, on ultrathin NaCl films on Au(111) by tip-induced dehalogenation of a decachlorofluorene ($C_{13}Cl_{10}$) precursor. AFM and STM provide insight into the geometry and electronic structure. We observe some C_{13} molecules with a pronounced kink, indicating a localized angular carbene center. At other adsorption sites, the kink was less pronounced, resulting in a rounder shape, and indicating that the extent of carbene localization depends on the local environment. Our results show that C_{13} has an open-shell triplet ground state with 13 electrons in both its π-systems. Taking advantage of the high reactivity of odd-number cyclocarbons, the larger cyclo[26]carbon (C_{26}) was formed through dehalogenation and dimerization of two $C_{13}Cl_{10}$ precursors. Orbital density maps of C_{26} visualize pairs of its energy degenerate molecular frontier orbitals, experimentally revealing its electronic structure.

On-surface synthesis of C_{13}

The precursor decachlorofluorene, $C_{13}Cl_{10}$ (Fig. 1A (top); for synthesis see figs. S1 to S3) was sublimed by fast heating from a Si wafer onto an Au(111) surface partially covered with monolayer and bilayer NaCl, at a sample temperature of about $T = 10$ K. Characterization by

STM and AFM in non-contact mode was performed with CO tip functionalization (*19*) at $T = 5$ K, typically on monolayer NaCl.
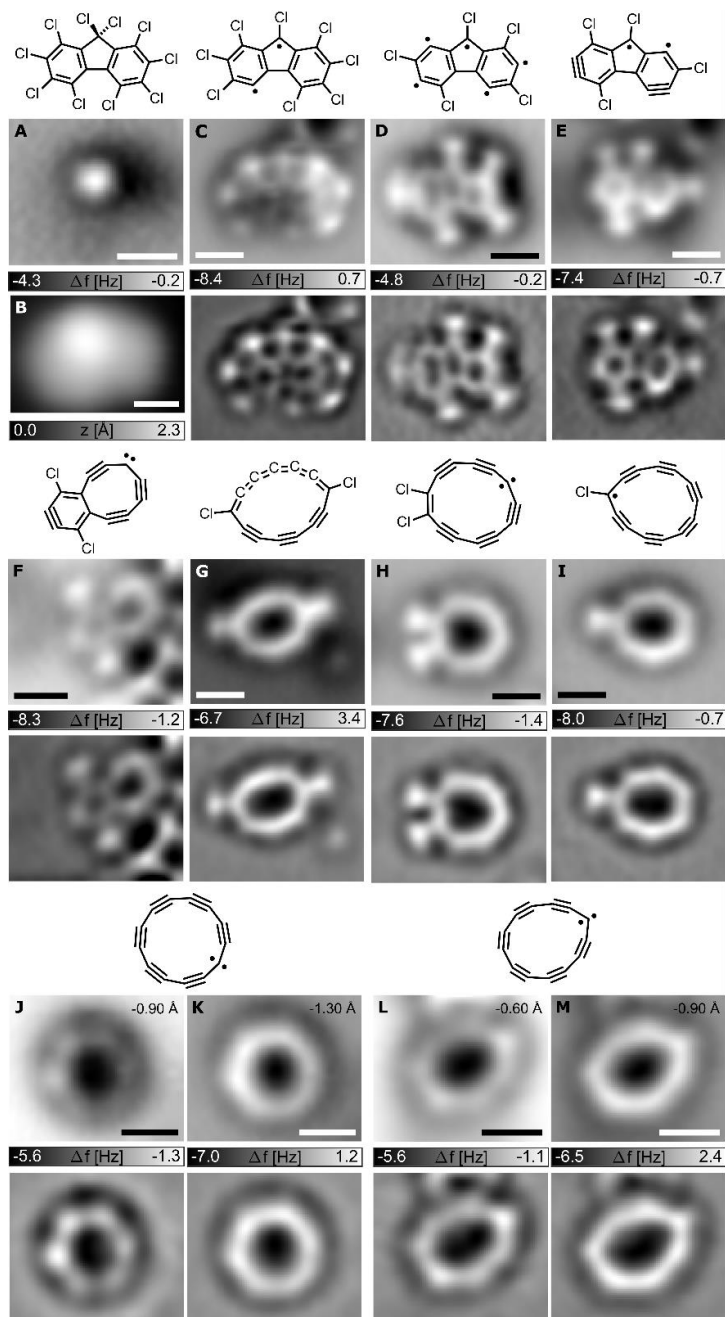
Fig. 1. On-surface synthesis of C$_{13}$. (**A**) Precursor, AFM data with a tip-height offset $\Delta z = 0.7$ Å from the setpoint of $V = 0.2$ V and $I = 0.5$ pA, and (**B**) STM data, $V = 0.2$ V, $I = 0.5$ pA. (**C** to **I**) Intermediates observed after applying voltage pulses on precursors. AFM raw data in upper panels and Laplace-filtered data in the respective lower panels. Tentatively assigned Kekulé structures are shown above each panel. (**J** to **M**) Two individual C$_{13}$ molecules, with different structural distortion, i.e., "round" (J and K) and "kinked" (L and M), at AFM-far (J and L) and AFM-close (K and M) with tip-height offsets Δz indicated. All scale bars 5 Å.

3

We found intact precursor molecules as shown in Fig. 1A and B. Because of its non-planarity, we only observe one bright feature in AFM (Fig. 1A), at the position of a protruding Cl atom bonded to the sp^3 hybridized C atom of the central CCl_2 unit. Voltage pulses of up to $V = 4.5$ V with currents I on the order of a few pA, applied for a few 100 ms, were used to unmask precursor molecules by dehalogenation on monolayer NaCl. Usually, voltage pulses resulted in partial dehalogenation and Fig. 1, C to I show some of the observed intermediates indicating that retro-Bergman reactions ([21, 22]) were induced. Successively applied voltage pulses led to C_{13}, see Fig. 1, J to M and figs. S4 to S12. We generated 16 individual C_{13} molecules on the surface with a yield of about 40%. In unsuccessful attempts, the ring opened to form linear or branched polyynic chains (see fig. S7) or the molecule was picked up by the tip. Up to two Cl adatoms could be reversibly reattached ([23]) to C_{13}, resulting in structures such as shown in Fig. 1, G, H and I (see also fig. S6). We observed C_{13} in a range of different shapes, varying from a "round", see Fig. 1, J and K to a more distorted, "kinked" geometry see Fig. 1, L and M (see also figs. S8 to S12). All results show measurements on monolayer NaCl. On bilayer NaCl, dehalogenated products could only be stably imaged in few cases without moving them (see fig. S9), indicating a small diffusion barrier.
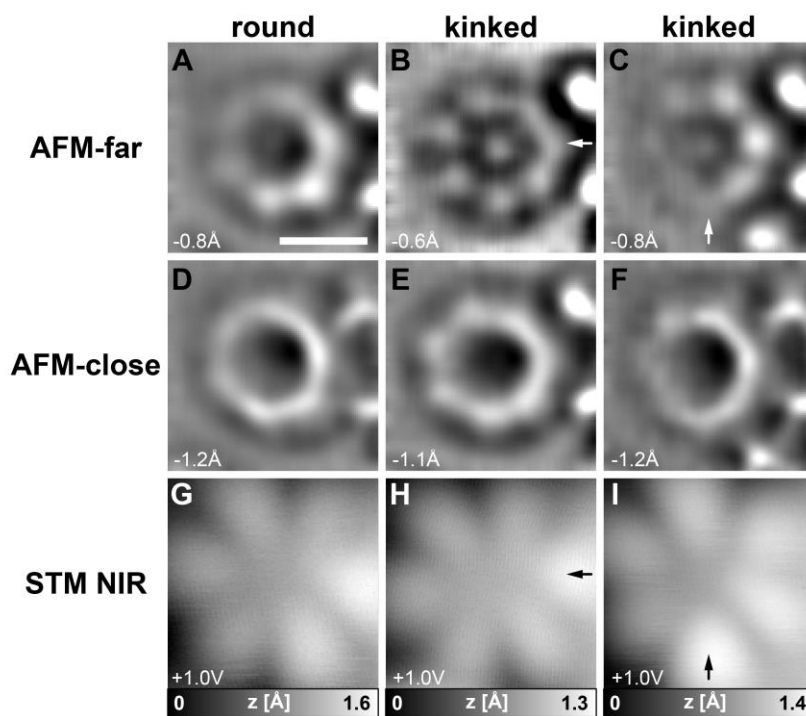

Fig. 2. Electronic characterization of C_{13}. (**A-C**) AFM-far, (**D-F**) AFM-close, Δz indicated. Laplace-filtered data, for raw data, see fig. S11. (**G-I**) STM data, $V = 1.0$ V, $I = 0.5$ pA. All panels show the same individual molecule, adsorbed on ML NaCl at three different sites next to a BL NaCl step-edge, which is located on the right-hand side in all panels. For the "kinked" C_{13} (2nd and 3rd column), the location of the kink is indicated by arrows. Scale bar 5 Å, applies to all images.

The extent of distortion in individual C_{13} molecules was different at different adsorption sites (see Fig. 2 and figs. S8 to S12), indicating that the shape is influenced by the surface environment (*2*). "Round" C_{13} exhibit six bright lobes in AFM-far, see Fig. 1J, while in AFM-close they show pronounced edges on one side of the ring and a rounder shape on the opposing side, see Fig. 1K. The more distorted, "kinked" C_{13} exhibit seven lobes in AFM-far, see Fig. 1L, while at AFM-close they exhibit the shape of a squeezed heptagon, see Fig. 1M.

Figure 2 shows AFM and STM data of the same individual C_{13} molecule at different adsorption sites next to a NaCl bilayer island. In Fig. 2A the molecule exhibits "round" and in Fig. 2, B and C, "kinked" shapes. We observed that the degree of kinking varies smoothly across different environments, rather than defining two discrete geometries (see also fig. S12). At the bilayer step-edge, the molecule was adsorbed with sufficient stability to obtain STM maps at the negative ion resonance (NIR), i.e., transiently attaching an electron into a low-energy unoccupied molecular orbital (*24*), shown in Fig. 2, G to I. For all observed shapes, the STM maps show six lobes of high orbital density. Observing similar orbital densities points towards the C_{13} molecules having the same electronic state, despite adopting different geometries (*25*).

Theory results on C$_{13}$

Cyclocarbons exhibit two orthogonal π-systems: one "in-plane" with orbital lobes in the plane of the nuclei (shown in orange in Fig. 3A) and one "out-of-plane" with zero density in the molecular plane (blue in Fig. 3A). Thus, four π-orbitals are near the Fermi energy (*8, 13*). C_{13} has six electrons in these four frontier orbitals, giving rise to several possible electronic ground states. We label these states according to the occupation of their frontier in-plane orbitals (first two numbers) and out-of-plane orbitals (second two numbers). In an infinitely large ring with no BAA, the two π-systems are degenerate. However, in a finite ring, the out-of-plane π-system becomes slightly lower in energy than its in-plane counterpart (*13*) and in the absence of both BLA and BAA (D_{13h} geometry), the higher-lying in-plane orbitals *A′* and *B′* will be singly occupied, while their out-of-plane counterparts *A″* and *B″* will be doubly occupied, resulting in a triplet ground state $^3|11\ 22\rangle$, see Fig. 3B.
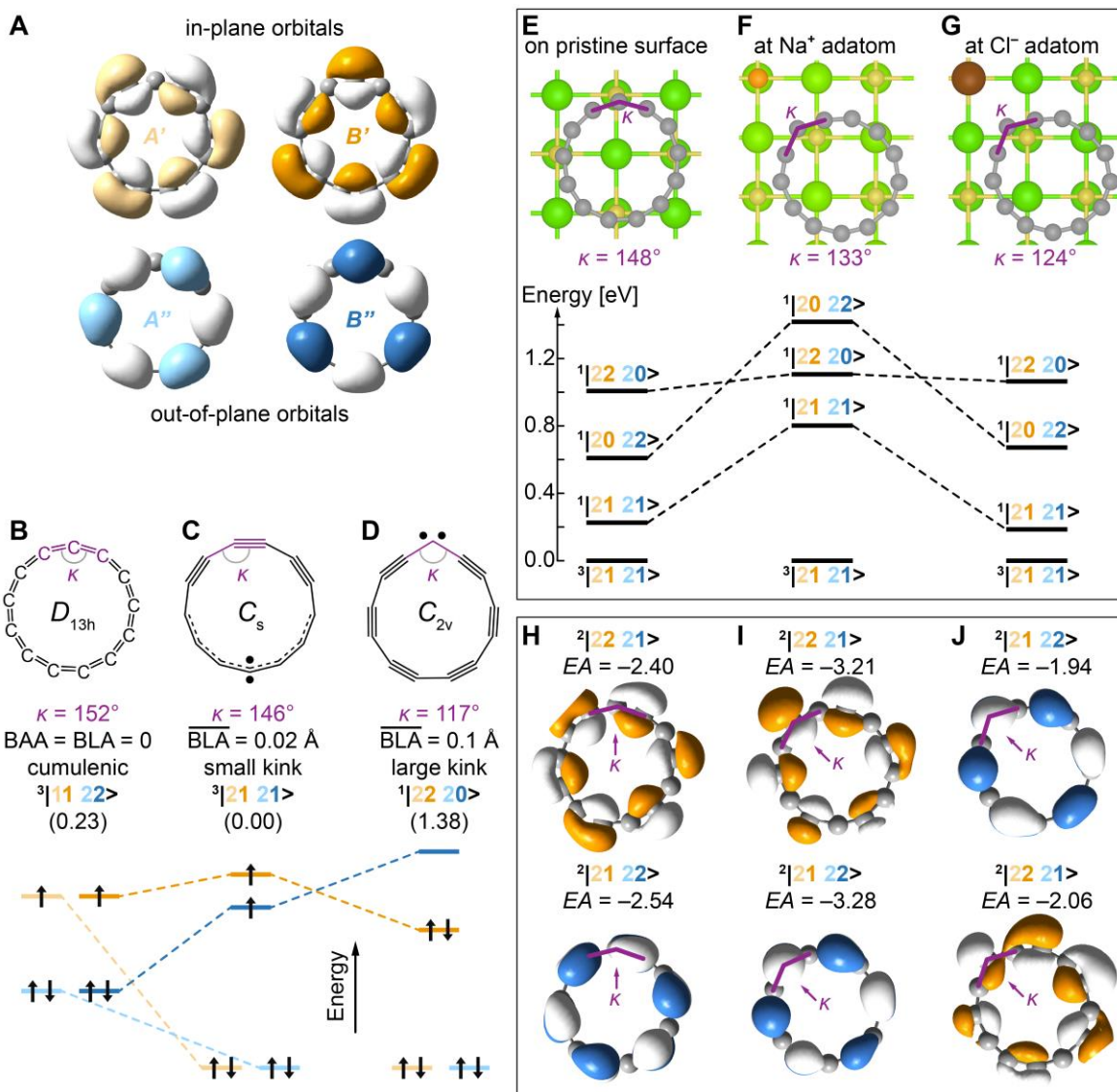
Fig. 3. **Theoretical investigation of C_{13}**. (**A**), Frontier orbitals of C_{13} in D_{13h} geometry. (**B** to **D**), CASPT2 optimized geometries and relative energies (in eV) of C_{13} in the gas phase, with averaged BLA indicated. (**B**) a D_{13h} cumulenic structure, (**C**) the $^3|21\ 21>$ triplet state, which is found to be the ground state, (**D**) the $^1|22\ 20>$ closed-shell singlet state. (**E** to **G**) On-surface calculations for C_{13}, (**E**) on a pristine NaCl surface, (**F**) Next to a positively charged adatom, and (**G**) next to a negatively charged adatom. Energies of several singlet states, relative to the $^3|21\ 21>$ triplet ground state, are indicated. (**H-J**) Dyson orbitals for the transitions to the two lowest anionic charge states from the $^3|21\ 21>$ state in the geometries of (E to G) respectively, with electron affinity (*EA*) in eV indicated. (For more theory results see figs. S13 to S17).

Introducing BLA lowers the energy of *A* orbitals and increases the energy of their *B* counterparts. This results in the triplet $^3|21\ 21>$ ground state, see Fig. 3C, with 13 electrons in both π-systems, which adopts a shape with a small kink (the smallest bond angle is $\kappa = 146°$, smaller than $\kappa = 152°$ for the D_{13h} geometry) and an irregular pattern of BLA. A structure with a larger kink ($\kappa = 117°$) can be found by optimizing the geometry of the $^1|22\ 20>$ closed-shell singlet state, see Fig. 3D. The $^3|21\ 21>$ and $^1|22\ 20>$ states were found with similar energies by Baryshnikov et al.

(*12*), with CASSCF and DFT calculations. The ^{3}|21 21> open-shell structure with a small kink (Fig. 3C) can be considered a delocalized *sp* carbene. The ^{1}|22 20> closed-shell structure (Fig. 3D) can be described as a localized sp^2 carbene, contributing the lone electron pair in its sp^2 hybridized orbital to the in-plane system, and an empty *p* orbital to the out-of-plane system (*12*).

5   Our CASPT2 (complete active space perturbation theory) calculations (details in Methods Section), which add dynamic correlation on top of a self-consistent CAS wavefunction, indicate that the triplet ^{3}|21 21> state is the global minimum of C_{13}, both in the gas phase (Fig. 3C) and for different adsorption environments on the NaCl surface (Fig. 3, E to G). Explicitly correlated coupled clusters calculations, also predict a triplet ground state (fig. S17).

10   In the gas phase (Fig. 3C) and on a pristine surface (Fig. 3E), the C_{13} at its triplet minimum exhibits a small kink (κ = 146–148°) and small BLA. The kink becomes more pronounced when the molecule interacts with surface defects, such as adatoms (Fig. 3, F and G) and the spin density becomes more localized at the kink (fig. S15), but the ground state remains ^{3}|21 21>. In all considered geometries, the states with closed-shell configurations as major contributions are more than 0.6 eV above the triplet ground state (Fig. 3, E to G). DFT calculations on all
15   optimized geometries found C_{13} to be antiaromatic in its ^{3}|21 21> state.

Electronic characterization of C_{13}

The STM maps of the NIR (Fig. 2, G to I) can be compared to calculated Dyson orbitals for
20   electron attachment $<\psi^{n+1}|\psi^n>$, where *n* is the number of electrons (*26, 27*). Vertical attachment of an electron to C_{13} in the triplet ground state $\psi^n = {}^3$|21 21> can result in an electronic state with doubly occupied out-of-plane orbitals $\psi^{n+1} = {}^2$|21 22> or doubly occupied in-plane orbitals $\psi^{n+1} = {}^2$|22 21>. Electron affinities (*EA*) for inserting an electron in the in-plane and out-of-plane system are very similar (within ~0.15 eV), with more kinked geometries energetically favoring
25   electron attachment to the in-plane π-system (see fig. S14).

The Dyson orbitals of both transitions are shown in Fig. 3, H to J (for the respective on-surface geometries see fig. S14 and for Dyson orbitals calculated using a quantum-computing algorithm see fig. S16). Because of the energy broadening of the ionic resonances on NaCl of about 0.3 eV (*24*) and the larger extension of the out-of-plane orbitals towards the tip than the in-plane
30   orbitals, we expect that the respective out-of-plane Dyson orbitals (drawn in blue) dominate the STM contrast, and that the in-plane orbitals are challenging to resolve (see fig. S9). Although the geometric distortion does not change the nodal plane structure of the Dyson orbitals, it does affect the extent of delocalization (i.e. the intensity of the lobes) and ordering of the ^{2}|21 22> and ^{2}|22 21> states. In the case of a more pronounced kink, the Dyson orbital usually becomes more
35   localized at the kink (Fig. 3, H to J, and figs. S9, S14 and S16).

The "kinked" C_{13} is well described by adsorption next to a Cl^- adatom (Fig. 3J), as the NIR shows a more pronounced lobe above the kink (Fig. 2, H and I, and fig. S9) and the in-plane orbital is observed closer to the Fermi energy than the out-of-plane orbital (see fig. S9). The "round" C_{13} is well described by the C_{13} on the pristine surface (Fig. 3H). Lobes of the NIR are
40   between short bonds on the side of the molecule with strong BLA, i.e., the side that shows more pronounced edges in AFM-close (Fig. 2D).

Comparing experiment and theory, we conclude that the adsorbed C_{13} molecules are all in the triplet ^{3}|21 21> ground state with an *sp* carbene center, which makes them remarkably different from even-*N* cyclocarbons (*1-4*). C_{13} exhibits geometries with a differently pronounced kink,

7

indicating various degrees of localization of the carbene center, depending on the surface environment. While the carbene is delocalized over several carbon sites in the "round" C_{13}, it is localized to a specific carbon in the "kinked" C_{13}.

Dimerization to C_{26}

Applying voltage pulses above two neighboring C_{13} precursors on the surface yielded the molecule shown in Fig. 4 (see also figs. S18 to S21), which we assign as C_{26}, a cyclo[N]carbon of the $N = (4k + 2)$ series. The AFM contrast (Fig. 4, A and B, see also fig. S19) indicates pronounced BLA, and thus a polyynic structure (Fig. 4C).
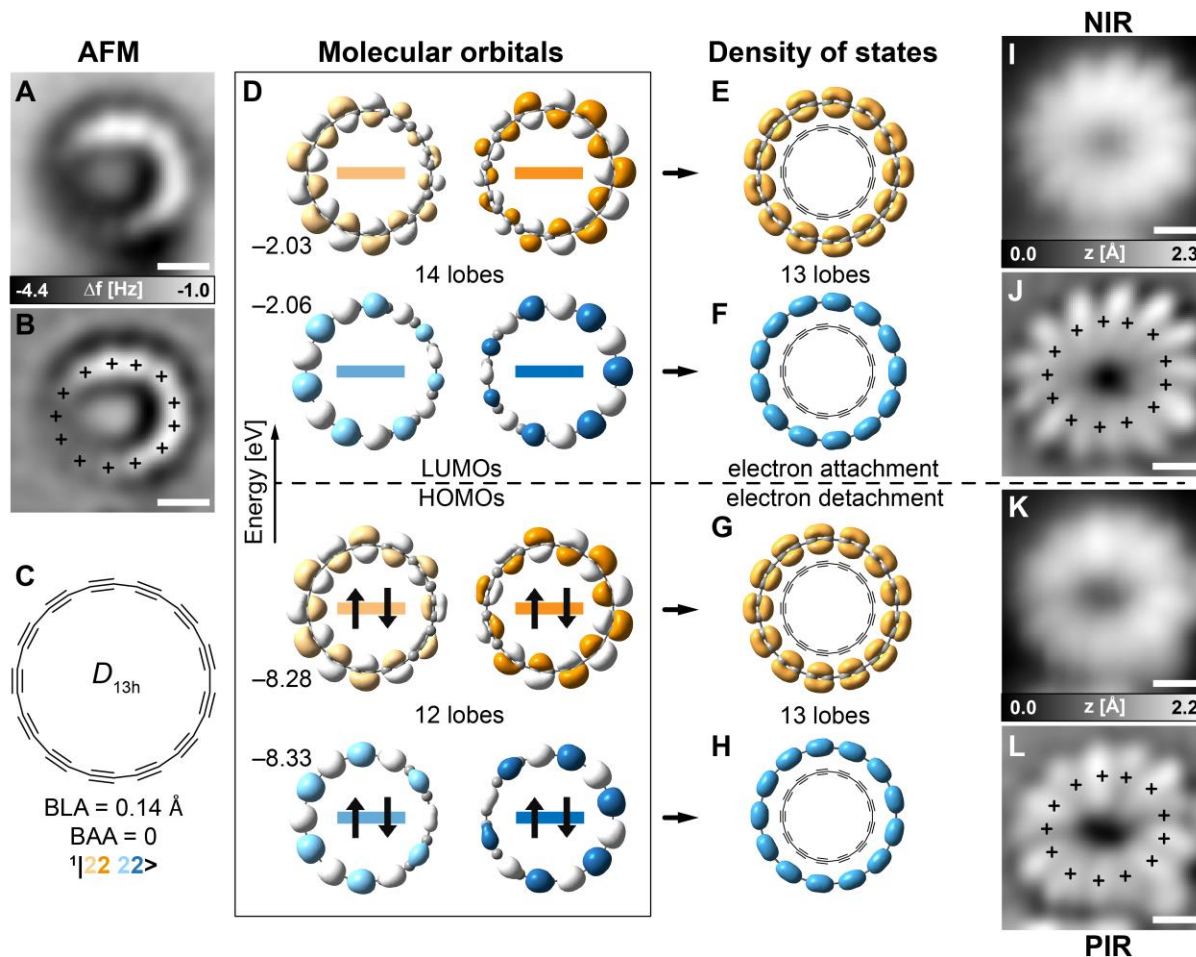
Fig. 4. Cyclo[26]carbon. (**A**) AFM data and (**B**) corresponding Laplace-filtered data, with the positions of the bright features, indicating short bonds, marked. (**C** to **H**) DFT calculations in the gas phase. (**D**) Frontier molecular orbitals, with energies in eV indicated. (**E** to **H**) Superposition of orbital densities of the respective energy degenerate orbital pairs shown in (D). (**I** and **J**) STM data at NIR, $V = 2.0$ V, $I = 0.5$ pA; (**K** and **L**) STM data at PIR, $V = -2.75$ V, $I = 0.5$ pA. (J and L) Laplace-filtered images of (I and K) with the positions of the short bonds, obtained by AFM (B), marked. Scale bars 5 Å.

By STM we resolve orbital densities of this $(4k + 2)$ cyclocarbon, see Fig. 4. In agreement with theory (Fig. 4, D to H), the STM maps for both NIR, imaged at $V = 2.0$ V (Fig. 4, I and J) and

positive ion resonance (PIR) imaged at $V = -2.75$ V (Fig. 4, K and L), show 13 lobes. For the NIR, the lobes of high density are located above the long bonds (between the marks in Fig. 4J), as expected from a superposition (28) of the energy-degenerate lowest unoccupied molecular orbitals (LUMOs), which have 14 lobes each (see Fig. 4F). For the PIR, the lobes are located above the short bonds (on the marks in Fig. 4L) and could result from the superposition of the densities of the energy-degenerate highest occupied molecular orbitals (HOMOs), see Fig. 4G. However, as explained above for the case of C_{13}, out-of-plane orbitals will dominate the STM contrast, because they expose a larger orbital density towards the tip than the in-plane orbitals and are almost energy degenerate with them. Like the in-plane HOMOs, the out-of-plane HOMOs (HOMO–2 and HOMO–3) of C_{26} have 12 lobes each, the superposition of which yields 13 lobes above short bonds (Fig. 4H). Tunnelling dominantly into the exposed out-of-plane HOMOs at the PIR explains why the cylindrical nodal plane along the ring of the in-plane HOMOs is not observed in the STM map of the PIR (Fig. 4, K and L), similar to measurements on C_{20} (4). The observation of the ionic resonances being superpositions of the densities of two orbitals results from the energy degeneracy of the respective two orbitals (28), and confirms the doubly aromatic, closed-shell singlet configuration of C_{26}.

The high reactivity of odd-N C_{13} probably makes it favorable for two C_{13} molecules to fuse and form C_{26}. The on-surface synthesis of C_{26} indicates that odd-N cyclocarbons, due to their extremely high reactivity, allow the creation of larger novel carbon allotropes (29).

References

[1]   Kaiser, K., Scriven, L. M., Schulz, F., Gawel, P., Gross, L., and Anderson, H. L. An *sp*-hybridized molecular carbon allotrope, cyclo[18]carbon. *Science* **365**, 1299–1301 (2019).

[2]   Gao, Y., Albrecht, F., Rončević, I., Ettedgui, I., Kumar, P., Scriven, L. M., Christensen, K. E., Mishra, S., Righetti, L., Rossmannek, M., et al. On-surface synthesis of a doubly anti-aromatic carbon allotrope. *Nature* **623**, 977–981 (2023).

[3]   Sun, L., Zheng, W., Gao, W., Kang, F., Zhao, M., and Xu, W. Aromatic annular carbon allotropes: cumulenic cyclo[10]carbon and Peierls-transition-intermediate cyclo[14]carbon. *Nature* **623**, 972–976 (2023).

[4]   Sun, L., Zheng, W., Kang, F., Gao, W. and Xu, W., On-surface synthesis and characterization of anti-aromatic cyclo[12]carbon and cyclo[20]carbon, PREPRINT (Version 2) available at Research Square [https://doi.org/10.21203/rs.3.rs-3411934/v2] (2023)

[5]   Diederich, F., Rubin, Y. Knobler, C. B., Whetten, R. L., Schriver, K. E., Houk, K. N., and Li, Y. All-carbon molecules: evidence for the generation of cyclo [18] carbon from a stable organic precursor. *Science* **245**, 1088–1090 (1989).

[6]   Chen, X., Yan, X., Liu, Z., Yuan, T., Bu, C., Shang, Y., Xiao, H., Wu, Y., Wei, H., and Xu, J. Chemistry of cyclo-[2n]-carbon: A many-particle quantum mechanics investigation. *PREPRINT ChemRxiv 10.26434/chemrxiv-2023-plj1t-v2* (2023).

[7]   Hoffmann, R. *Tetrahedron* **22**, 521–538 (1966).

[8]   Fowler, P. W., Mizoguchi, N., Bean, D. E., and Havenith, R. W. A. Double aromaticity and ring currents in all-carbon rings. *Chem. Eur. J.* **15**, 6964–6972 (2009).

[9]   Brito, B., Hai, G.-Q., and Cândido, L. Quantum Monte Carlo study on the structures and energetics of cyclic and linear carbon clusters C_n ($n = 1,..., 10$). *Phys. Rev. A* **98**, 062508 (2018).

[10]   Yen, T. and Lai, S. Use of density functional theory method to calculate structures of neutral carbon clusters C_n ($3 \leq n \leq 24$) and study their variability of structural forms. *J. Chem. Phys.* **142**, 084313 (2015).

[11]   Baryshnikov, G. V., Valiev, R. R., Nasibullin, R. T., Sundholm, D., Kurten, T., and Ågren, H. Aromaticity of even-number cyclo[*n*]carbons ($n = 6$–100). *J. Phys. Chem. A* **124**, 10849–10855 (2020).

[12]   Baryshnikov, G. V., Valiev, R. R., Valiulina, L. I., Kurtsevich, A. E., Kurtén, T., Sundholm, D., Pittelkow, M., Zhang, J., and Ågren, H. Odd-number cyclo[*n*]carbons sustaining alternating aromaticity. *J. Phys. Chem. A* **126**, 2445–2452 (2022).

[13]   Rončević, I., Leslie, F. J., Rossmannek, M., Tavernelli, I., Gross, L., and Anderson, H. L. Aromaticity reversal induced by vibrations in cyclo[16]carbon. *J. Am. Chem. Soc.* **145**, 26962–26972 (2023).

[14]   Anderson, H. L., Patrick, C. W., Scriven, L. M., and Woltering, S. L. A short history of cyclocarbons. *Bull. Chem. Soc. Jpn.* **94**, 798–811 (2021).

[15]   Tobe, Y. and Wakabayashi, T. Polyynes: synthesis, properties, and applications, Ch. 6, Ed. Cataldo, F., CRC Press (2005).

[16]   Marlton, S. J., Buntine, J. T., Watkins, P., Liu, C., Jacovella, U., Carrascosa, E., Bull, J. N., and Bieske, E. J. Probing colossal carbon rings. *J. Phys. Chem. A* **127**, 1168–1178 (2023).

[17]   Wang, S., Rittby, C., and Graham, W. Detection of cyclic carbon clusters. I. Isotopic study of the $v_4(e')$ mode of cyclic C_6 in solid Ar. *J. Chem. Phys.* **107**, 6032–6037 (1997).

[18]   Clair, S. and de Oteyza, D. G. Controlling a chemical coupling reaction on a surface: tools and strategies for on-surface synthesis. *Chem. Rev.* **119**, 4717–4776 (2019).

[19]   Gross, L., Mohn, F., Moll, N., Liljeroth, P., and Meyer, G. The Chemical Structure of a Molecule Resolved by Atomic Force Microscopy. *Science* **325**, 1110–1114 (2009).

[20]   Scriven, L. M., Kaiser, K., Schulz, F., Sterling, A. J., Woltering, S. L., Gawel, P., Christensen, K. E., Anderson, H. L., and Gross, L. Synthesis of cyclo[18]carbon via debromination of $C_{18}Br_6$. *J. Am. Chem. Soc.* **142**, 12921–12924 (2020).

[21]   Schuler, B., Fatayer, S., Mohn, F., Moll, N., Pavliček, N., Meyer, G., Peña, D. and Gross, L. Reversible Bergman cyclization by atomic manipulation. *Nat. Chem.* **8**, 220–224 (2016).

[22]   Lee, J. K., Lee, G. D., Lee, S., Yoon, E., Anderson, H. L., Briggs, G. A. D., and Warner, J. H. Atomic scale imaging of reversible ring cyclization in graphene nanoconstrictions. *ACS Nano* **13**, 2379–2388 (2019).

[23]   Pavliček, N., Schuler, B., Collazos, S., Moll, N., Pérez, D., Guitián, E., Meyer, G., Peña, D., and Gross, L. On-surface generation and imaging of arynes by atomic force microscopy. *Nat. Chem.* **7**, 623–628 (2015).

[24]   Repp, J., Meyer, G., Stojkovic, S. M., Gourdon, A., and Joachim, C. Molecules on Insulating Films: Scanning-Tunneling Microscopy Imaging of Individual Molecular Orbitals. *Phys. Rev. Lett.* **94**, 026803 (2005).

[25]   Mishra, S., Vilas-Varela, M., Lieske, L.-A., Ortiz, R., Rončević, I., Albrecht, F., Frederiksen, T., Peña, D., and Gross, L. Bistability between π-diradical open-shell and closed-shell states in indeno[1,2-*a*]fluorene. *arXiv preprint arXiv*:2303.04483 (2023).

[26]   Pomogaev, V., Lee, S., Shaik, S., Filatov, M., and Choi, C. H. Exploring Dyson's orbitals and their electron binding energies for conceptualizing excited states from response methodology. *J. Phys. Chem. Lett.* **12**, 9963–9972 (2021).

[27]   Ortiz, J. Dyson-orbital concepts for description of electrons in molecules. *J. Chem. Phys.* **153**, 070902 (2020).

[28]   Pavliček, N., Mistry, A., Majzik, Z., Moll, N., Meyer, G., Fox, D. J., and Gross, L. Synthesis and characterization of triangulene. *Nat. Nano.* **12**, 308–311 (2017).

[29]   Diederich, F. Carbon scaffolding: building acetylenic all-carbon and carbon-rich compounds. *Nature* **369**, 199–207 (1994).

[30]   Giessibl, F. J. Atomic resolution on *Si*(111)-7×7 by noncontact atomic force microscopy with a force sensor based on a quartz tuning fork. *Appl. Phys. Lett.* **76**, 1470–1472 (2000).

[31]   Albrecht, T. R., Grütter, P., Horne, D., and Rugar, D. Frequency modulation detection using high-Q cantilevers for enhanced force microscope sensitivity. *J. Appl. Phys.* **69**, 668–673 (1991).

[32]   Gross, L., Mohn, F., Moll, N., Schuler, B., Criado, A., Guitián, E., Peña, D., Gourdon, A., Meyer, G. Bond-Order Discrimination by Atomic Force Microscopy. *Science*. **337**, 1326–1329 (2012).

[33]   Hapala, P, Kichin, G., Wagner, C., Tautz, F. S., Temirov, R. and Jelínek, P. The mechanism of high-resolution STM/AFM imaging with functionalized tips. *Phys. Rev. B*. **90**, 85421 (2014).

[37]   Fdez. Galván, I. et al. OpenMolcas: From source code to insight. *J. Chem. Theory. Comput.* **15**, 5925–5964 (2019).

[38]   Kendall, R. A., Dunning Jr, T. H., and Harrison, R. J. Electron affinities of the first-row atoms revisited. Systematic basis sets and wave functions. *J. Chem. Phys*. **96**, 6796–6806 (1992).

[39]   Finley, J., Malmqvist, P.-Å., Roos, B. O., and Serrano-Andrés, L. The multi-state CASPT2 method. *Chem. Phys. Lett.* **288**, 299–306 (1998).

[40]   Chai, J. D. and Head-Gordon, M. Long-range corrected hybrid density functionals with damped atom–atom dispersion corrections. *Phys. Chem. Chem. Phys.* **10**, 6615–6620 (2008).

[41]   Weigend, F. and Ahlrichs, R. Balanced basis sets of split valence, triple zeta valence and quadruple zeta valence quality for H to Rn: Design and assessment of accuracy. *Phys. Chem. Chem. Phys.* **7**, 3297–3305 (2005).

[42]   Frisch, M. J. et al. Gaussian 16 Rev. C.01, Wallingford, CT (2016).

[43]   Martin, C. W., Gill, H. S. and Landgrebe, J. A. Diaryldichlorocarbonyl ylides derived from dichlorocarbene and aromatic ketones. *J. Org. Chem.* **48**, 1898–1901 (1983).

[44]   Soya, T., Mori, H. and Osuka, A. Quadruply twisted Hückel-aromatic dodecaphyrin. *Angew. Chem. Int. Ed.* **57**, 15882 (2018).

11

[45]   Li Manni, G., Fdez. Galvan I. *et al.*, The OpenMolcas Web: A Community-Driven Approach to Advancing Computational Chemistry. *J. Chem. Theory Comput.* **19**, 6933 (2023).

[46]   Ibe Y., Nakagawa Y. O., Earnest N., Yamamoto T., Mitarai K., Gao Q., and Kobayashi T. Calculating transition amplitudes by variational quantum deflation. *Phys. Rev. Res.* **4**, 013173 (2021).

[47]   Oana, C. M., and Krylov A. I., Dyson orbitals for ionization from the ground and electronically excited states within equation-of-motion coupled-cluster formalism: Theory, implementation, and examples. *J. Chem. Phys.* **127**, 234106 (2007).

[48]   Guo, Y., Riplinger, C., Becker, U., Liakos, D. G., Minenkov, Y., Cavallo, L., Neese, F. Communication: An improved linear scaling perturbative triples correction for the domain based local pair-natural orbital based singles and doubles coupled cluster method [DLPNO-CCSD(T)]. *J. Chem. Phys.* **148**, 011101 (2018).

[49]   Hättig, C., Klopper, W., Köhn, A., Tew, D. P. Explicitly correlated electrons in molecules. *Chem. Rev.* **112**, 4-74 (2012).

[50]   Kong, L., Bischoff, F. A., Valeev, E. F. Explicitly correlated R12/F12 methods for electronic structure. *Chem. Rev.* **112**, 75-107 (2012).

[51]   Neese, F., Wennmohs, F., Becker, U., Riplinger, C. The ORCA quantum chemistry program package. *J. Chem. Phys.* **152**, 224108 (2020).

Author contributions: Conceptualization: FA, HLA, LG

Synthesis of the precursors: YG

On-surface synthesis and STM/AFM measurements: FA, FP, SM, LG

Theoretical analysis and computational simulations: IR, AB, IT

Writing: All authors.

Competing interests: The authors declare that they have no competing interests.

Data and materials availability: All experimental data are reported in the main text and supplementary materials. Additional data, i.e., results of calculations, are deposited at Zenodo.

Supplementary Materials

Materials and Methods

Supplementary Text

Figs. S1 to S21

References (*30-51*)

Supplementary Material for

The odd-number cyclo[13]carbon and its dimer cyclo[26]carbon

Florian Albrecht,[1][†] Igor Rončević,[2][†] Yueze Gao[2][†], Fabian Paschke[1][†], Alberto Baiardi[3], Ivano Tavernelli[3], Shantanu Mishra[1], Harry L. Anderson[2]* and Leo Gross[1]*

[1] IBM Research Europe – Zürich, 8803 Rüschlikon, Switzerland.

[2] Department of Chemistry, Oxford University, Chemistry Research Laboratory, Oxford, United Kingdom.

[3] IBM Quantum, IBM Research Europe – Zürich, 8803 Rüschlikon, Switzerland.

† These authors contributed equally.

*Corresponding authors. Email: harry.anderson@chem.ox.ac.uk; lgr@zurich.ibm.com

Contents

1. STM and AFM methods

The on-surface characterization and reactions were performed in a home-built combined STM/AFM, operated at a temperature of 5 Kelvin in ultra-high vacuum. The precursor, i.e., decachlorofluorene, was thermally sublimed onto a cold ($T < 10$ K) Au(111) surface partially covered with NaCl islands of one (ML) and two (BL) atomic layers thickness. AFM measurements were performed in non-contact mode with a qPlus sensor (*30*). The sensor was operated in frequency modulation mode (*31*) with the oscillation amplitude kept constant at 0.5 Å. If not noted otherwise, all data were recorded on molecules adsorbed on ML NaCl on Au(111) with CO functionalized tips. STM images were recorded at constant current and AFM images at constant height. The STM controlled setpoint for constant-height AFM images was $I = 1.0$ pA and $V = 0.2$ V if not mentioned otherwise. Positive (negative) tip-height offsets Δz correspond to an increase (decrease) in tip-sample distance with respect to the setpoint. In the AFM images of the intermediates, shown in Fig. 1, Δz was selected to result in bond resolved contrast. Typically, that is achieved at a maximal frequency shift Δf of about 0 Hz in the AFM image. With AFM-far we denote an imaging height (Δz) just at the onset of atomic resolution. That is, Δz chosen as large as possible to still yield bond resolved contrast. With AFM-close, we denote imaging at Δz further reduced by about 0.3 Å, with respect to AFM-far. At AFM-far, bond-order related contrast is usually observed as brightness contrast in the Δf-map, while at AFM close, due to CO-tip relaxations (*32, 33*), bond-order related contrast is observed in the apparent bond length (*32*). The latter results in apparent corners at the position of triple bonds in polyynic cyclocarbons (*1, 20*). AFM images were acquired at $V = 0$ V. The bias voltage V was applied to the sample with respect to the tip. Voltage pulses to induce dehalogenation were applied at constant height for a few 100 ms, with the tip being retracted by 6 to 8 Å from a setpoint of $I = 1$ pA and $V = 0.2$ V, resulting in currents I on the order of few pA.

2. Computational methods

All multireference calculations were done using OpenMolcas (*37*). The geometry of C_{13} was optimized at the CASPT2(6,8)/cc-PVTZ level of theory (*38*), which included all $k = 3$ (six lobes) and $k = 4$ (eight lobes) orbitals in the active space. We targeted the first triplet root, and both lowest singlets in a state-averaged two-state calculation. In the gas phase, the major contributions to the lowest triplet and singlet were both |21 21>, giving very similar round geometries (Fig. 3C), while the second singlet state, ^{1}|22 20>, optimized to a strongly kinked geometry (Fig. 3D). The (100) NaCl surface was simulated with an array of immobile point charges with a lattice parameter of 2.72 Å, following prior work (*2*). On each of the calculated surfaces (Fig. 3, E to G), we found very similar relaxed geometries of C_{13} in its different electronic states, respectively. This indicates that on-surface geometries depend more strongly on the surface environment than on the chosen electronic state.

Single-point energies of optimized geometries were evaluated at the multistate (*39*) CASPT2(12,14)/cc-PVTZ with four states; for the anions, the (13,14) space was used. This active space captures all $\Delta k = 0$ and $\Delta k = \pm 1$ transitions involving frontier orbitals (*13*) and it was used in previous investigations of C_{13} (*12*).

The geometry minimum and electronic structure of C_{26}, as well as the aromaticity of C_{13}, was calculated at ωB97XD/def2-TZVP (40, 41), following prior work (11, 12), using the Gaussian16 program (42).

3. Synthetic general methods

Reagents were purchased reagent-grade from commercial suppliers and used without further purification. $MgSO_4$ was used as the drying reagent after the aqueous work-up. Thin layer chromatography (TLC) was carried out on aluminium-backed silica gel plates with 0.2 mm thick silica gel 60 F254 (Merck) and visualized via UV-light (254/364 nm). Flash column chromatography was either carried out using flash silica gel 60 (230-400 mesh) obtained from Sigma-Aldrich. ^{1}H and ^{13}C NMR spectra were recorded on Bruker AVIII HD 500 spectrometers at 500 MHz (^{1}H) and 126 MHz (^{13}C) at 298 K. NMR chemical shifts are reported in ppm relative to $SiMe_4$ ($\delta = 0$) and were referenced internally with respect to residual solvent protons using the reported values (^{1}H: $CDCl_3$: 7.26 ppm; ^{13}C: $CDCl_3$: 77.16 ppm). All chemical shifts are reported in ppm, coupling constants are reported in Hz and ^{1}H multiplicities are reported in accordance with the following: s = singlet; d = doublet; t = triplet; and m = multiplet.

Synthetic protocols:
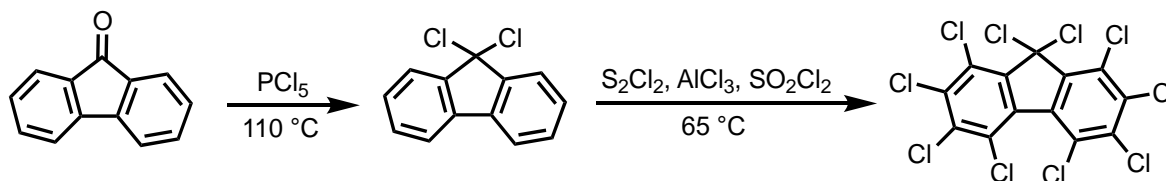
9,9-Dichlorfluorene. (43) 9H-Fluoren-9-one (1.00 g, 5.55 mmol) and PCl_5 (1.73 g, 8.32 mmol) were mixed and stirred at 110 °C for 16 hours. After cooling to room temperature, CH_2Cl_2 (30 mL) was added. The reaction mixture was quenched by slowly adding aqueous saturated Na_2CO_3 solution (20 mL) at 0 °C. H_2O (20 mL) was added, the layers were separated, and the aqueous phase was extracted with CH_2Cl_2 (2 × 40 mL). The organic phases were combined, washed with brine (20 mL), dried ($MgSO_4$), and filtered. Solvent removal and purification by recrystallization (diethyl ether) afforded **9,9-dichlorfluorene** (340 mg, 1.45 mmol, 26%) as a white solid. **^{1}H NMR** (500 MHz, $CDCl_3$) δ 7.84–7.82 (m, 1H), 7.62–7.60 (m, 1H), 7.45–7.39 (m, 2H). **^{13}C NMR** (126 MHz, $CDCl_3$) δ 146.9, 136.7, 130.8, 129.2, 124.8, 120.3, 83.1.

Decachlorofluorene. To a suspension of $AlCl_3$ (851 mg, 6.38 mmol) in SO_2Cl_2 (75 mL) was added a solution of 9,9-dichlorfluorene (100 mg, 0.425 mmol) in S_2Cl_2 (2.0 mL, 25 mmol) and SO_2Cl_2 (25 mL) over 20 min via a syringe pump. In the meantime, the solution was stirred at 65 °C. After the completion of the addition, the solution was stirred at 65 °C for 16 h. After cooling to room temperature, CH_2Cl_2 (30 mL) was added. The mixture was slowly added into water at 0 °C, followed by quenching with aqueous saturated Na_2CO_3 solution (ca. 300 mL). The layers were separated, and the aqueous phase was extracted with CH_2Cl_2 (2 × 150 mL). The organic phases were combined, washed with brine (20 mL), dried ($MgSO_4$), and filtered. Solvent removal and washing with CH_2Cl_2 (8 mL) afforded decachlorofluorene as a white powder. The solvent was removed from the residual solution and the resulting solid was washed with diethyl

ether (20 mL). These two batches of decachlorofluorene (180 mg, 0.352 mmol, 83%) were combined as a white powder. **¹H NMR** (500 MHz, CDCl₃) No signals from the product were observed. **¹³C NMR** (126 MHz, CDCl₃) δ 142.2, 138.0, 136.5, 133.4, 130.6, 127.5, 81.1.

4. NMR Spectra

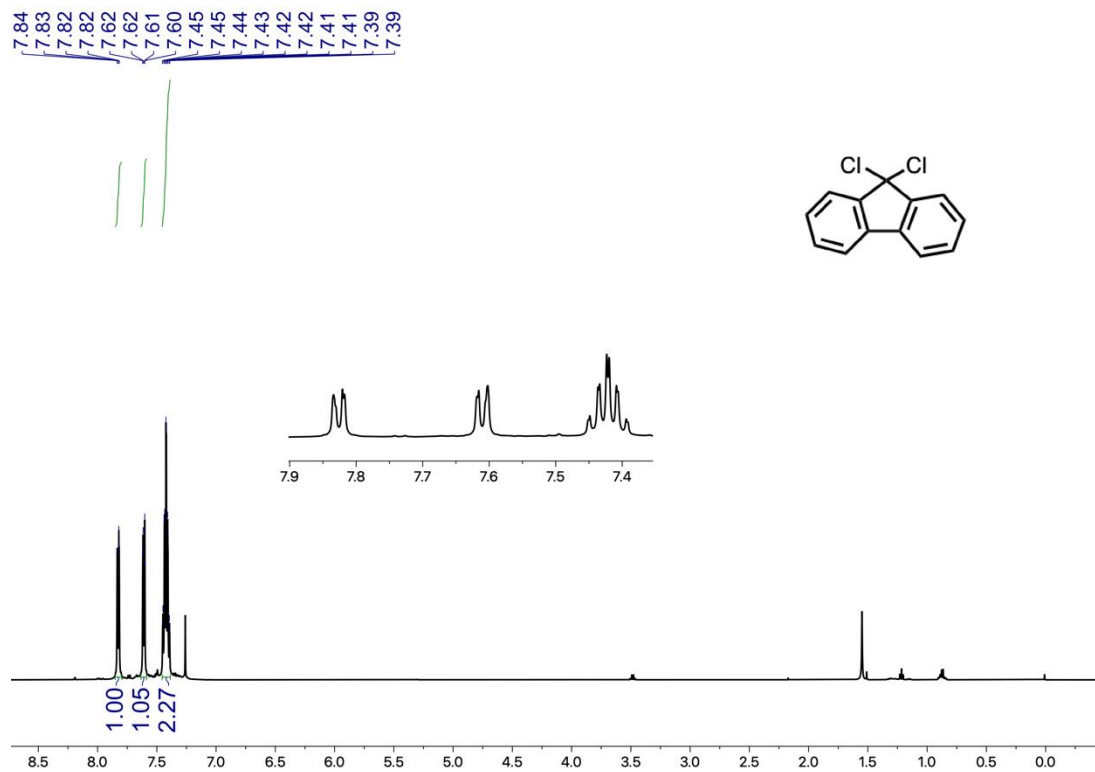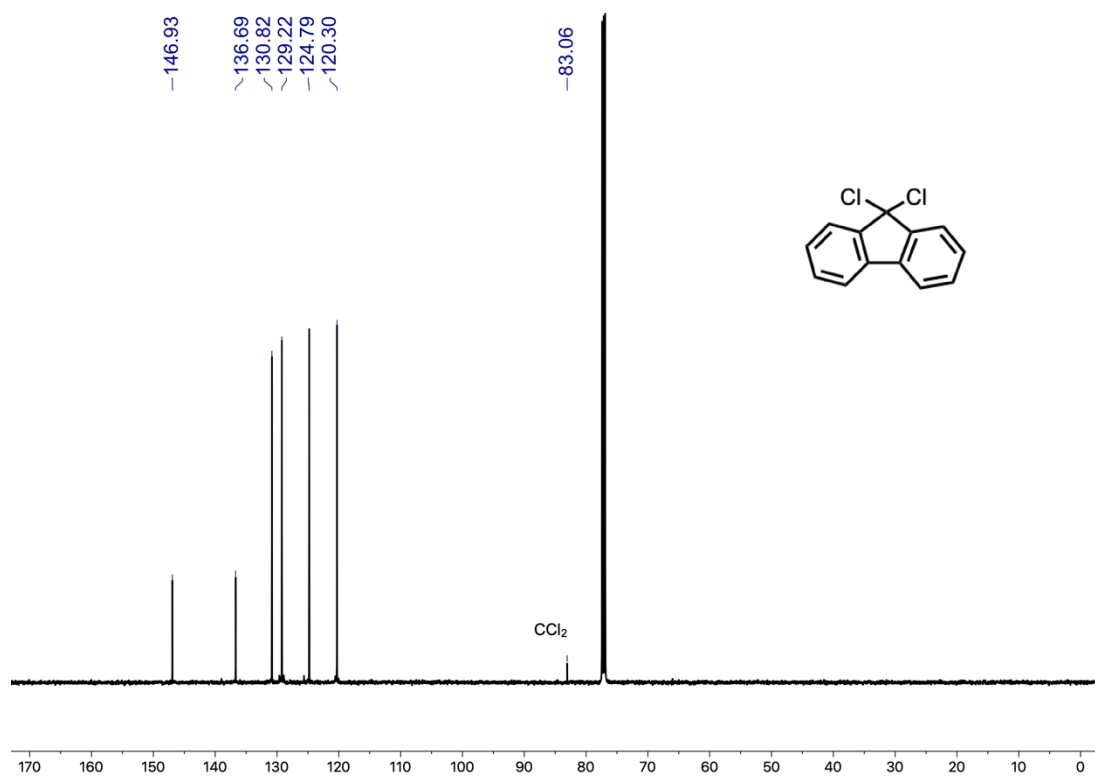**Figure S1.** ¹H NMR (500 MHz) spectrum of compound 9,9-dichlorfluorene in CDCl₃.

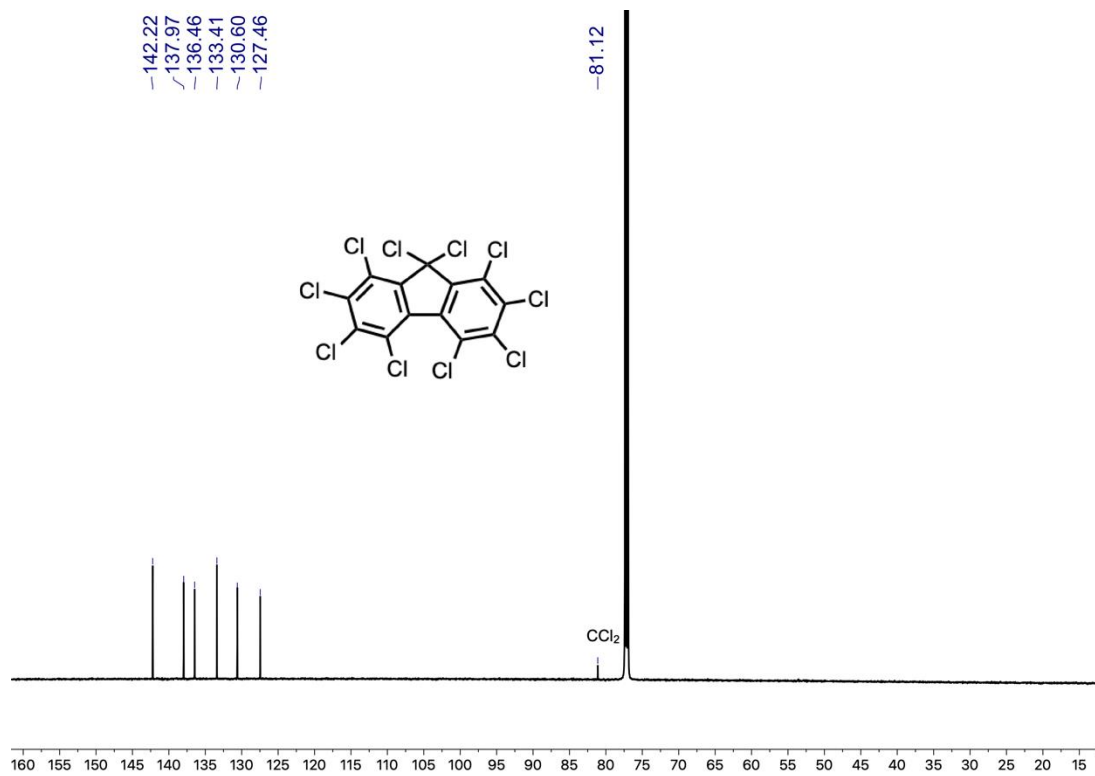**Figure S2.** ^{13}C NMR (126 MHz) spectrum of compound 9,9-dichlorfluorene in CDCl$_3$.

5

Figure S3. ^{13}C NMR (126 MHz) spectrum of compound decachlorofluorene in CDCl$_3$.

5. Additional experimental data on C_{13}
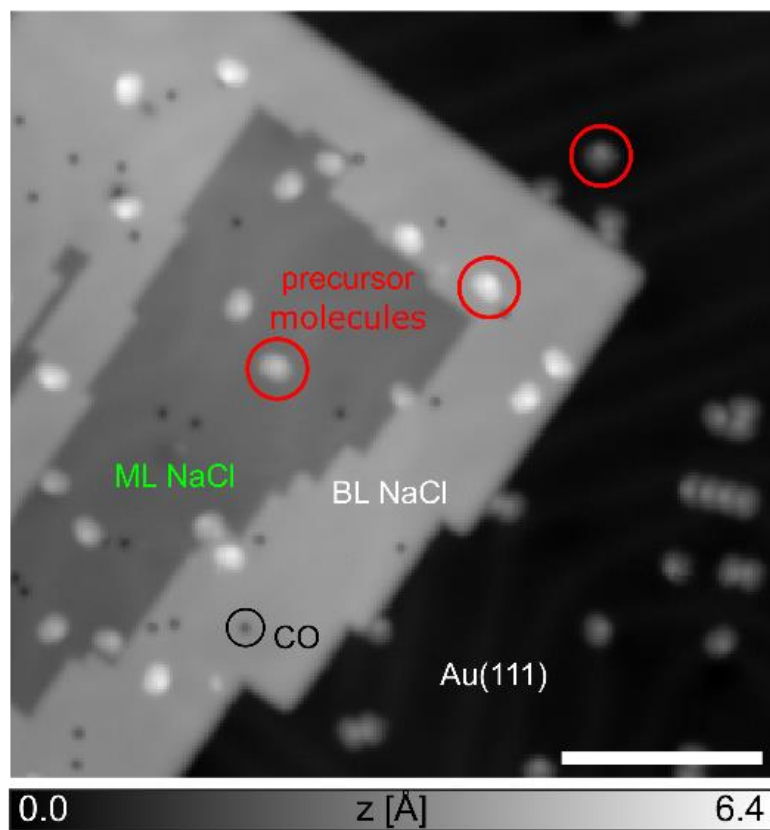
Figure S4. **STM overview image** ($V = 0.2$ V, $I = 0.5$ pA). A CO molecule, decachlorofluorene (precursor molecules for C_{13}), areas of bilayer (BL), monolayer (ML) NaCl islands and the uncovered Au(111) surface are indicated. Scale bar 100 Å.
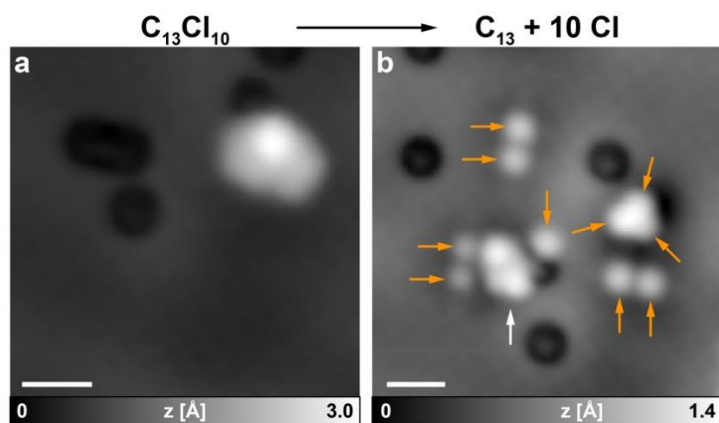
Figure S5. **STM images of C_{13} formation and dissociated chlorine atoms.** **(a)** STM image of individual precursor molecule adsorbed on ML NaCl next to a CO molecule. **(b)** After applying a voltage pulse of $V = 4.5$ V above the molecule shown in (a), with tip retracted by $\Delta z = 8$ Å from $V = 0.2$ V and $I = 1$ pA. The generated C_{13} is indicated by a white arrow, the ten dissociated chlorine atoms are indicated by orange arrows. Imaging parameters for both panels: $V = 0.2$ V, $I = 1$ pA. Scale bars 10 Å.
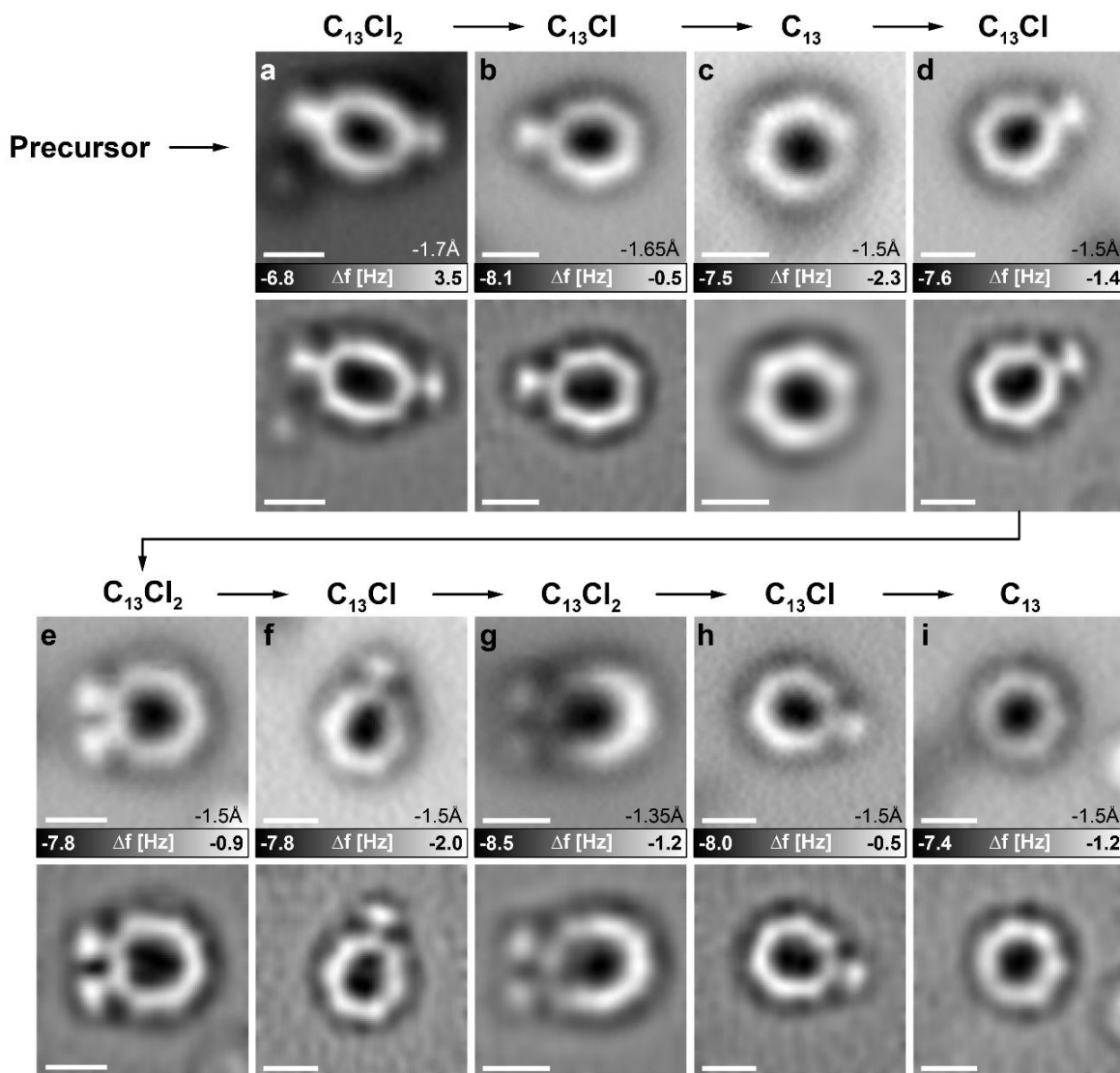
Figure S6. **Chlorination of a C_{13}.** AFM raw data (top) and corresponding Laplace-filtered images (bottom). Sequence of AFM images with voltage pulses ($V = 4$ to 4.5 V) applied above the molecule. **(a-c)** Dechlorination of $C_{13}Cl_2$ to C_{13}. **(c-e)** Chlorination of C_{13} to $C_{13}Cl_2$. **(e,f)** Dechlorination of $C_{13}Cl_2$ to $C_{13}Cl$. **(f,g)** Chlorination of $C_{13}Cl$ to $C_{13}Cl_2$. **(g-j)** Dechlorination of $C_{13}Cl_2$ to C_{13}. Indicated tip-height offsets Δz refer to a setpoint of $V = 0.2$ V, $I = 0.5$ pA, Scale bars 5 Å. Up to two Cl atoms, adsorbed near C_{13} on the NaCl surface, could reversibly be reattached to C_{13}.
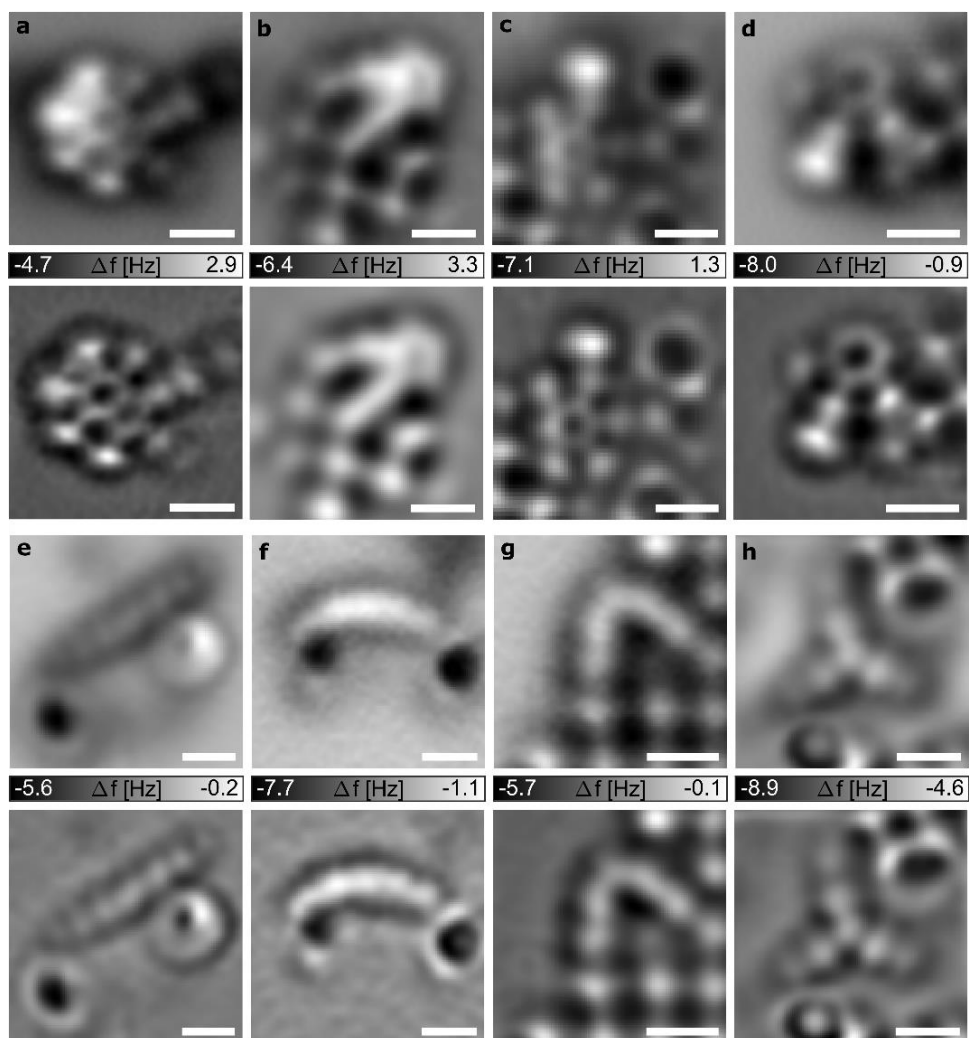
Figure S7. Unsuccessful results of attempted on-surface synthesis of C_{13}. Molecules observed after voltage pulses applied above decachlorofluorene that did not yield C_{13}. For each molecule (**a-h**), the AFM raw data is shown in the top panel and a corresponding Laplace-filtered image in the panel below. Molecules shown in (a, b, d, g) where adsorbed on bilayer NaCl, all other molecules on monolayer NaCl. We attempted generation of C_{13} on 41 individual decachlorofluorene precursors and successfully generated 16 individual C_{13} molecules resulting in a yield of about 40% for the on-surface synthesis. Scale bars 5 Å.
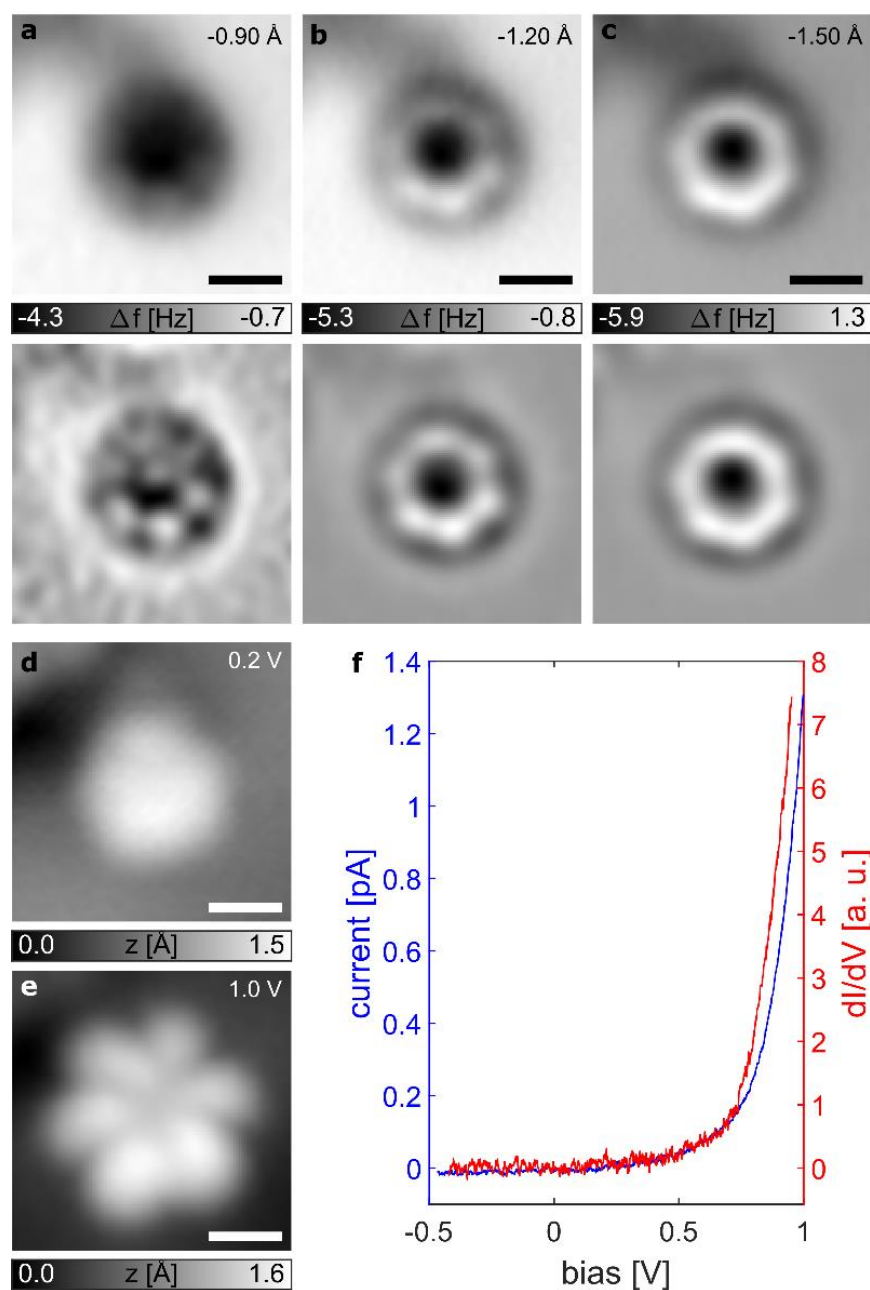
Figure S8. **Structural and electronic characterization of a "round" C_{13} on ML NaCl. (a-c)** AFM raw data and corresponding Laplace-filtered images below. Indicated tip-height offsets Δz refer to a setpoint of $V = 0.2$ V, $I = 0.3$ pA. (**d, e**) Constant-current STM images recorded at indicated voltages, $I = 0.3$ pA. (**f**) $I(V)$ spectrum (blue) and numerically derived dI/dV spectrum (red). All scale bars 5 Å.
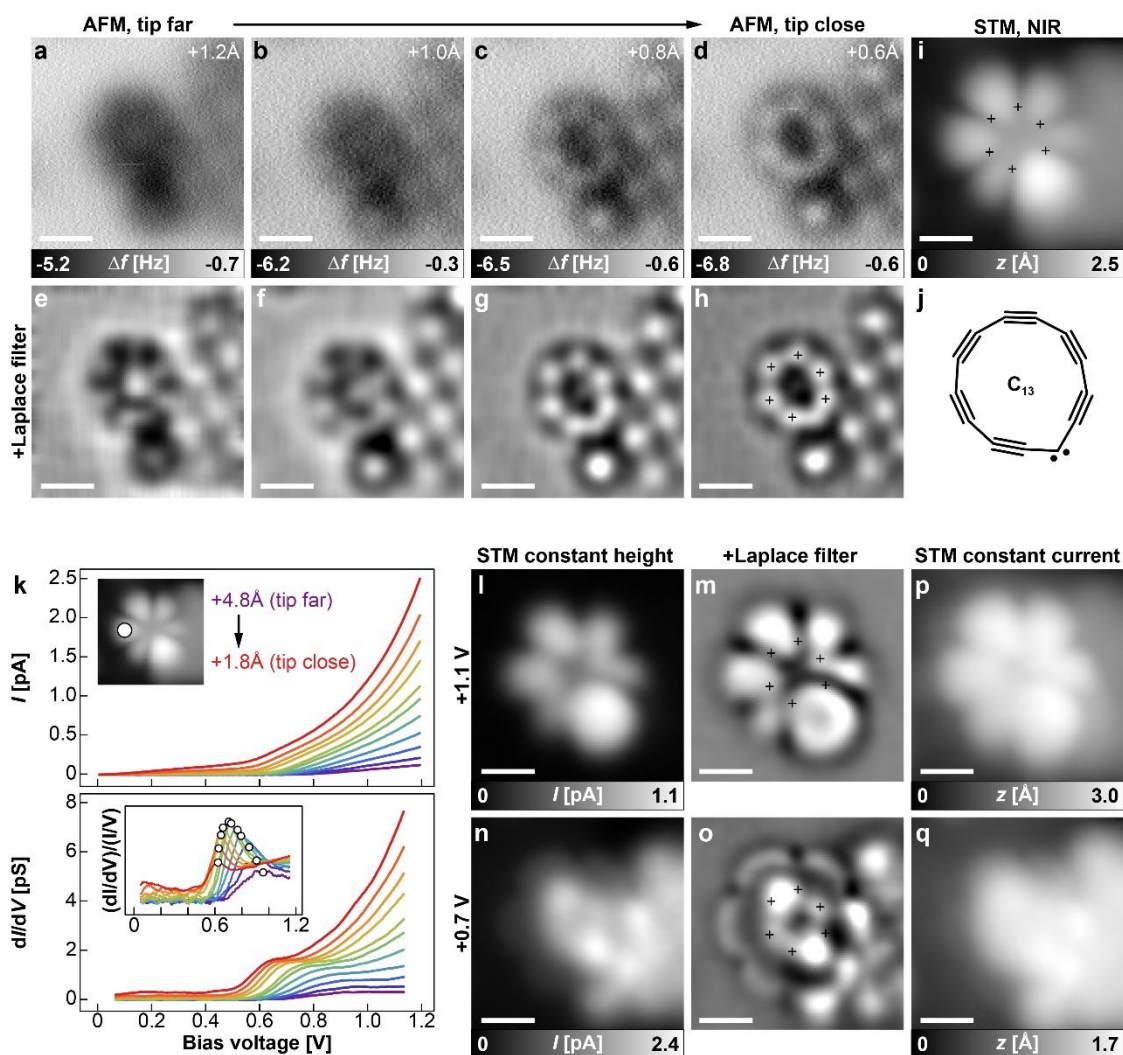
Figure S9. **Structural and electronic characterization of a "kinked" C_{13} on BL NaCl. (a-d)** AFM raw data and **(e-h)** corresponding Laplace-filtered images. C_{13} was stabilized at a third layer NaCl step edge. Indicated tip-height offsets Δz refer to a setpoint of $V = 0.2$ V, $I = 1.0$ pA on BL NaCl. **(i)** Constant-current STM image of the NIR recorded at $V = +0.8$ V and $I = 1.0$ pA. Crosses mark the bright spots in AFM-close, i.e., short bonds. **(j)** Corresponding orientation of the C_{13} on the surface. **(k)** $I(V)$ (top) and corresponding differential conductance dI/dV curves (bottom) recorded at the marked spot in the upper inset. Different tip heights are color-coded. Resonances in the dI/dV curves are highlighted by normalization on I/V (lower inset), and the peak positions are marked by circles. At larger tip heights (tip far), only one resonance at $V_1 = +1.1$ V is visible, whereas a second resonance appears upon tip approach (tip close), at about $V_2 = +0.7$ V. **(l-o)** Constant-height STM data (l, n) and Laplace-filtered images (m, o) recorded at resonances V_1 (l, m) and V_2 (n, o). The tip-height offsets Δz are +4.2 Å (top) and +1.8 Å (bottom) from a setpoint of $V = 0.2$ V, $I = 1.0$ pA on BL NaCl. Whereas V_1 depicts an out-of-plane orbital, the image at V_2 appears to be an in-plane-orbital. **(p, q)** Corresponding constant-current STM data, $I = 1.0$ pA. All scale bars are 5 Å.
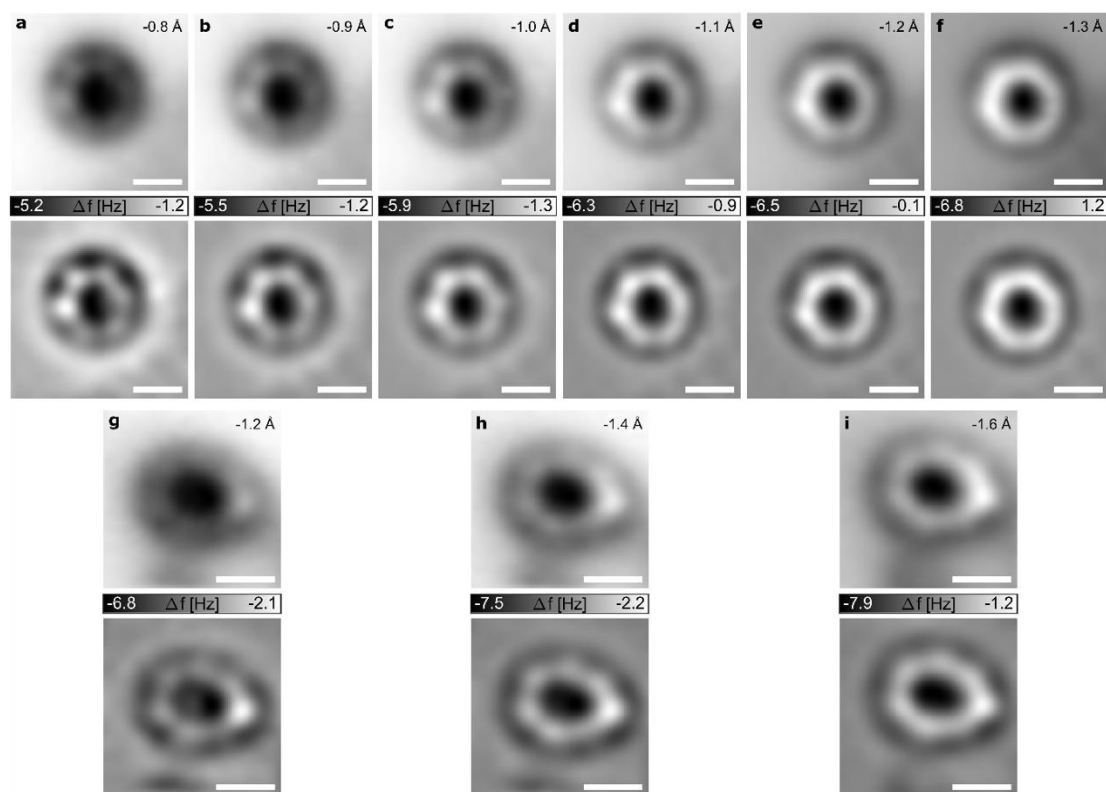
Figure S10. Additional AFM data on C_{13}. AFM images of a "round" (**a–f**) and a "kinked" (**g–i**) C_{13} molecule on ML NaCl. Raw AFM data is shown in upper panels and Laplace-filtered data is shown in the respective lower panels. Indicated tip-height offsets Δz refer to a setpoint of $V = 0.2$ V, $I = 1.0$ pA in (**a-f**) and of $V = 0.2$ V, $I = 0.5$ pA in (**g–i**). All scale bars 5 Å.
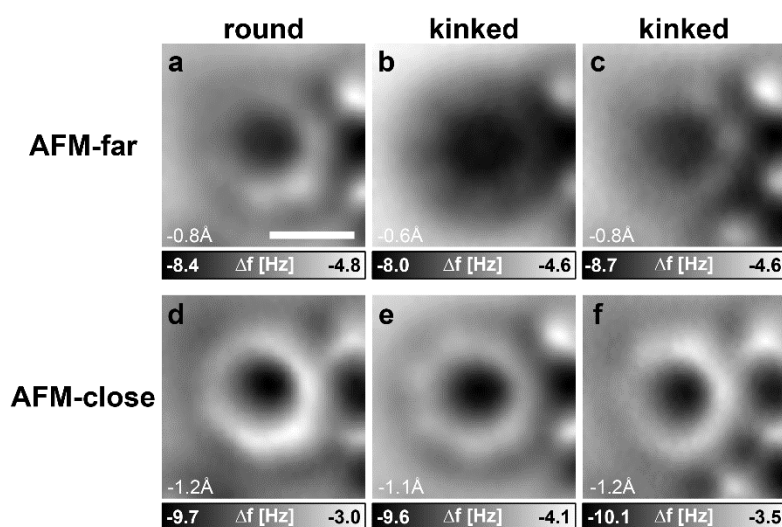

Figure S11. Raw AFM data of Fig. 2. Laplace-filtered images of this AFM data are shown in Fig. 2, A to F of the main text. (a–c) AFM-far, (d–f) AFM-close, with respective tip-height offset Δz indicated. Scale bar 5 Å, applies to all images.
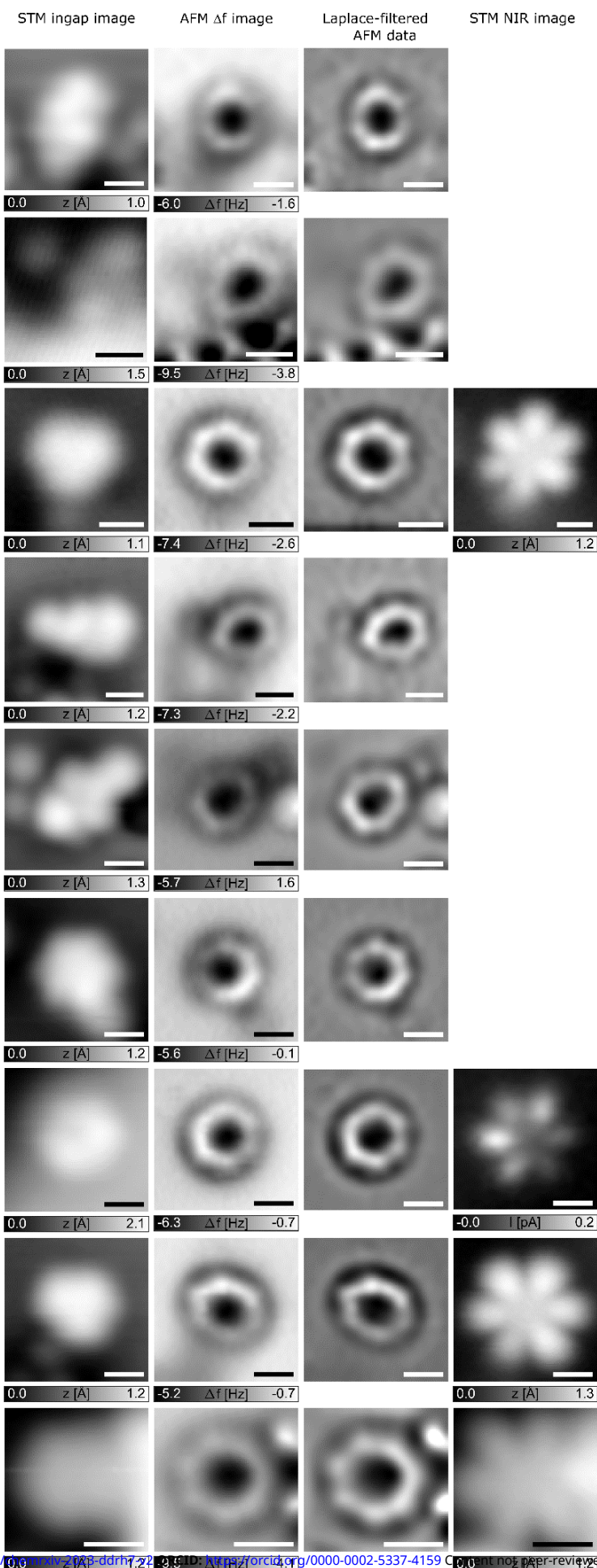
Figure S12. Additional AFM and STM data on different C_{13} molecules.

Experimental data of nine different individual C_{13} molecules. Each row shows the same individual molecule. The first column shows in-gap STM images ($V = 0.2$ V), the second column raw AFM data, the third column the respective Laplace-filtered AFM data. For the molecules that were adsorbed stably enough to obtain STM data at the NIR, the fourth column shows a STM image at $V = 1$ V. The NIR image in the third from bottom row was recorded in constant-height mode, all other STM images (including those shown in the main text) were acquired in constant-current mode. Scale bars 5 Å.

6. Computational details

Optimization. CASPT2 geometry optimizations of C_{13} were done in two steps. First, a rough optimization was performed with the default *SLAPAF* settings until the energy started oscillating. In the second step, the keywords *C2-DIIS*, *CARTESIAN*, and a smaller *MAXSTEP* (between 0.1 and 0.05, depending on the system) were added. This reduced the energy by an additional ~10 mHa relative to the first optimization, and usually resulted in an energy converging to within ~0.2 mHa. Point charges for the surface calculations, which included two layers (290 point-charges), were added via the *XFIELD* keyword.

The first CASSCF/CASPT2 triplet of C_{13} was always $^3|21\ 21>$. In a single-state singlet calculation, the first CASSCF/CASPT2 root was either $^1|22\ 20>$ (when the kink was large in the gas phase and at a positive adatom on surface) or $^1|20\ 22>$ (when the kink was small in the gas phase and on the pristine surface, and at a negative adatom on surface). In a two-state calculation the second CASSCF root (but lower in CASPT2 energy) was always $^1|21\ 21>$, optimizing to a geometry very similar to $^3|21\ 21>$ in all investigated environments. In the presence of point charges (on the surface), the optimized geometries of all three roots were very similar, with κ differing by about 1°.
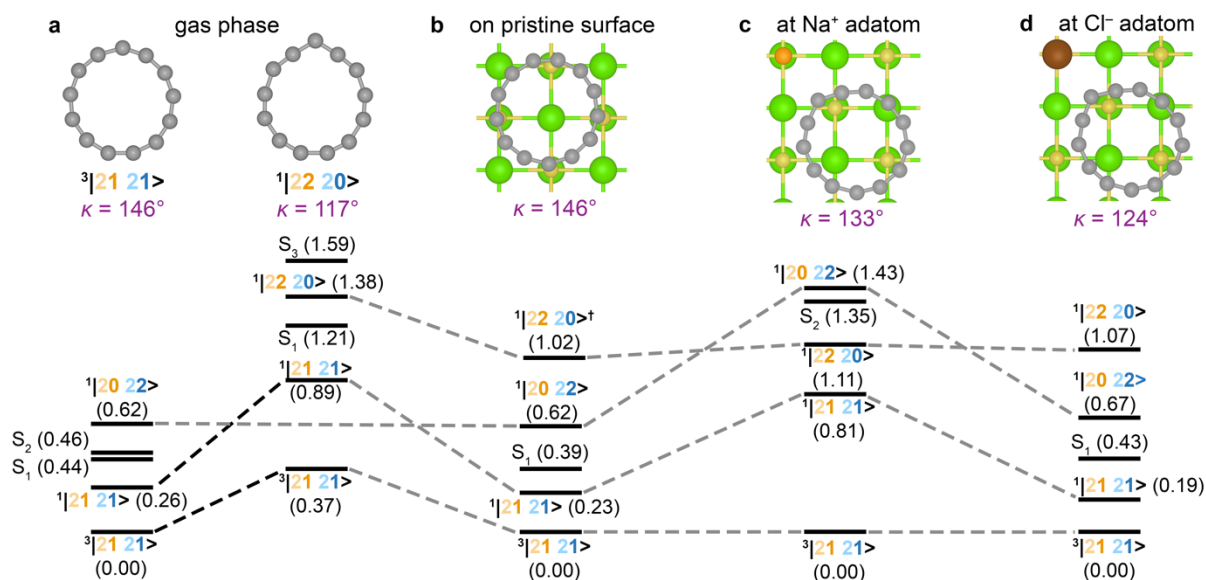

Figure S13. Electronic states and energies (in eV) of C_{13} calculated using multistate CASPT2. **a**, gas phase results at the optimized $^3|21\ 21>$ triplet and $^1|22\ 20>$ singlet geometry. **b–d**, on-surface results at the pristine surface (b) and at the positive (c) and negative (d) adatom, calculated at the optimized triplet geometry. Black lines connect states with similar composition in the same environment, and gray lines across different environments. †The $^1|22\ 20>$ state in (b) was not found at the optimized triplet geometry; the result shown is for the $^1|20\ 22>$ singlet optimized geometry with $\kappa = 145°$.

Single point CASPT2 energies. The combination of a triple-zeta basis set, large active space (14,12), and a multistate calculation with four roots resulted in significant multireference

character of all states. Energies of calculated states are compared in fig. S13. Shown at the triplet geometry (left hand side) and the |22 20> geometry (right-hand side) in fig. S13a, with approximate assignments of selected states. We note that the compositions of excited states are strongly dependent on the number of requested roots and the mixing scheme, i.e., state-averaged vs. multistate vs. extended multistate CASPT2, suggesting strong mixing between the states. A curiosity, which we noticed is that mixing the two closed-shell singlets, i.e., $\psi \approx {}^1|22\ 20> + {}^1|20\ 22>$, leads to a twisted Hückel topology (44).

Dyson orbitals were calculated from the self-consistent CASPT2 wavefunctions, using the *RASSI* module in OpenMolcas. In all cases, the Dyson norms were 0.85–0.92, indicating that little orbital relaxation occurs upon electron attachment, i.e. that $\psi^{n+1} \approx \psi^n\ \psi^{LUMO}$.

Effect of the kink. As indicated in Fig. 3, B and C, the kink affects the relative energies of the B′ and B″ orbitals. This is reflected in the ordering of the electron affinities for electron insertion into the out-of-plane π-system, which results in the ${}^2|21\ 22>$ state, and into the in-plane π-system, leading to ${}^2|22\ 21>$. However, as the energetic separation between them is small, the ordering of B′ and B″ orbitals has no considerable effect on the triplet ${}^3|21\ 21>$ ground state.
In the gas phase, when the kink is small ($\kappa \geq 133°$) the ${}^2|21\ 22>$ state (corresponding to electron attachment into the out-of-plane π-system) is lower in energy than ${}^2|22\ 21>$. As the distortion gets bigger ($\kappa < 133°$), the order reverses and the ${}^2|22\ 21>$ state (corresponding to electron attachment into the in-plane π-system) becomes lower in energy (fig. S14).

Increasing the kink localizes the spin density (fig. S15), also localizes the density for both in-plane and out-of-plane Dyson orbitals at the kink position (fig. S14). In correspondence, in the experiment, a lobe with increased density is observed above the kink for the "kinked" C_{13} (see Fig. 2, H and I).
In the optimized geometry on a pristine surface ($\kappa = 148°$, Fig. 3, E and H) and at a positively charged adatom ($\kappa = 133°$, Fig. 3, F and I) the electron affinity is lower (more negative) for inserting the electron in the out-of-plane π-system. Moreover, the Dyson orbital's density is more localized on the kink in the latter case. In the optimized geometry at a negatively charged adatom ($\kappa = 124°$, Fig. 3, G and J) inserting an electron in the in-plane system is energetically more favorable. At a negatively charged adatom, the density is not very localized at the kink due to Columbic repulsion, approximately compensating the effect of density localization due to the kink.

For the interpretation of the STM maps of the NIR of C_{13} (Fig. 2, G to I) it is important to consider that the tip, which is positioned above the ring, has a larger overlap of its wavefunctions with the out-of-plane system than with the in-plane system. Therefore, if transitions to both systems are possible (if their energy difference is smaller than, or similar to the peak broadening, which is 0.3 eV on NaCl (24)), tunneling into the out-of-plane system is expected to be the dominant channel for electron attachment. This explains why the NIR maps are expected to

28

correspond to out-of-plane Dyson orbitals, even if the in-plane orbital is slightly closer to the Fermi level, as is the case in Fig. 3J. The same argument explains why the PIR of C_{26} (Fig. 4L) appears in the shape of out-of-plane orbital densities (Fig. 4H).
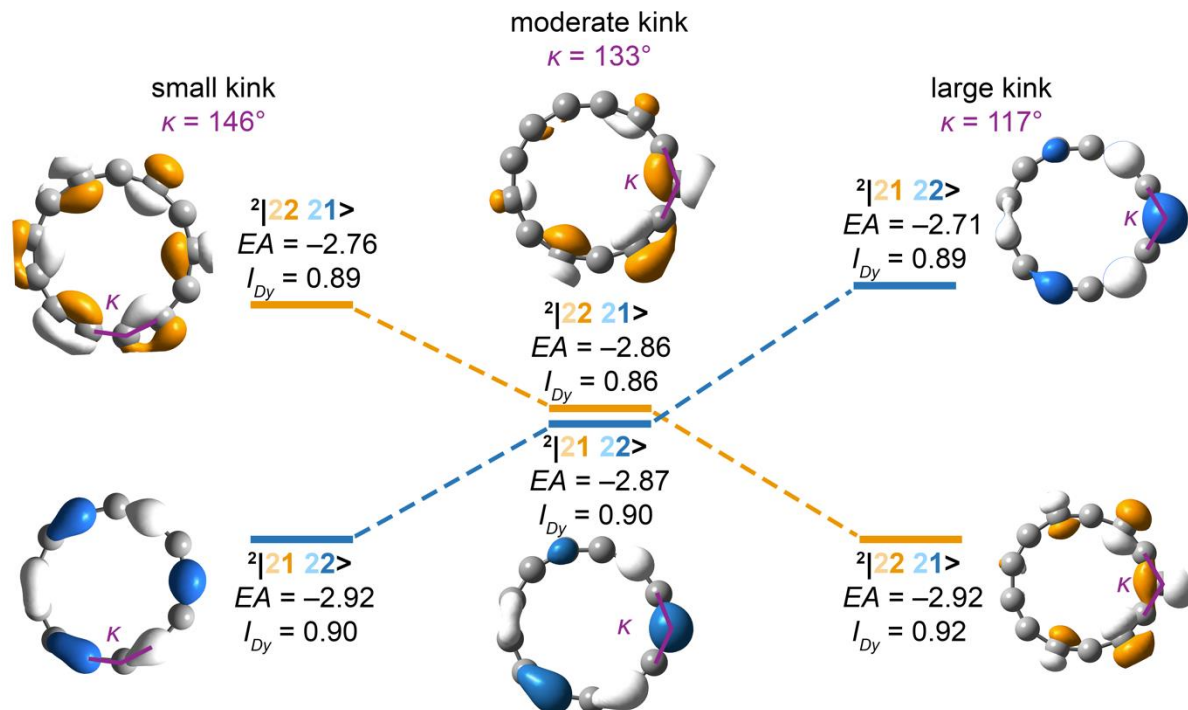
Figure S14. Dyson orbitals (at 0.05 a.u.) for electron attachment, their intensities (I_{Dy}) and electron affinities (EA) at three different kink values, calculated using CASPT2(12,14) in the gas phase.
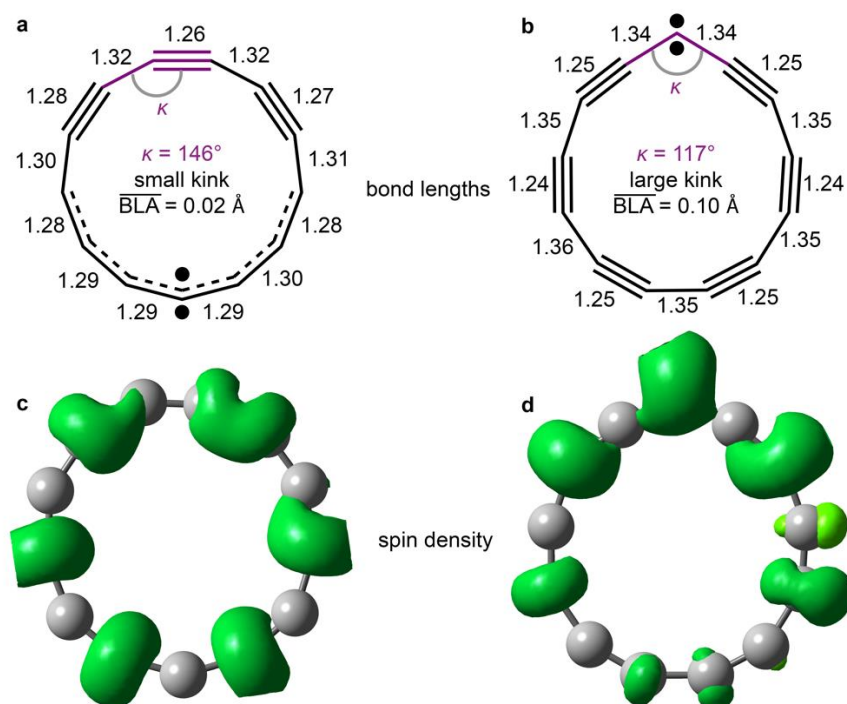
Figure S15. a,b, Bond lengths in Å. **c,d,** Spin densities of C_{13} in the ground triplet state at small (a,c) and large (b,d) kink values, calculated using CASPT2(12,14) in the gas phase. Spin density (green) at 0.005 a.u.

Quantum simulations. Following previous work of some of the authors (*2, 13*), we also employed quantum-computing. Here, we calculated Dyson orbitals using a quantum-computing algorithm. Specifically, we optimized the electronic wave function of C_{13} with the variational quantum eigensolver (VQE) based on the unitary coupled cluster with single and double excitations (qUCCSD) ansatz. All simulations were carried out with the statevector simulator as implemented in the Qiskit package. All qUCCSD calculations are based on the cc-pVTZ basis set, on an active space comprising 4 orbitals and 6 electrons, and on molecular orbitals optimized with the state-average complete active space self-consistent field algorithm as implemented in OpenMolcas (*45*) by averaging the electronic energy over the 5 lowest-energy states. In all cases, we included in the qUCCSD ansatz only excitation operators preserving the spin S_z operator (simulations including also spin-flip excitation operators yield the same qualitative trend discussed below).

qUCCSD predicts the ground state to be the closed-shell singlet $^1|22\ 20>$. This does not agree with the CASPT2 results, but matches the trend observed using CASSCF (*12*). This is to be expected since, as CASSCF, also qUCCSD neglects dynamical correlation effects, which are included in CASPT2. Nevertheless, as we show in fig. S16, qUCCSD correctly predicts the shape and relative energy ordering of the two lowest electron-affinity Dyson orbitals. The latter were obtained based on the lowest-energy triplet wave function, obtained by applying optimizing with VQE a qUCCSD ansatz constructed starting from a determinant composed of 4 alpha and 2 beta electrons, and the two lowest-energy anionic state, optimized with the variational quantum

deflation algorithm (*46*). We calculated the Dyson orbitals by converting the optimized qUCCSD wave functions to their statevector representation and, subsequently, applying the algorithm described in (*47*) for calculating Dyson orbitals based on configuration interaction-type wave functions. As we report in fig. S16, qUCCSD correctly predicts the relative energetic ordering of the Dyson orbitals both for the small-kink and for the large-kink geometries. In agreement with the CASPT2 results, the lowest electron affinity Dyson orbital is out-of-plane for the small kink value, and in-plane for the large kink value. This indicates that dynamical correlation does not play a crucial role in predicting the qualitative shape of the Dyson orbitals. The latter can, therefore, be efficiently predicted with quantum-computing simulations, which can efficiently capture strong, static correlation effects.

We note that, although in this work we used classical simulators of the quantum-computing calculation, it would be possible to calculate the Dyson orbitals directly on quantum hardware based on the algorithm described in (*12*). Moreover, we note that this is, up to our knowledge, the first proposal for a quantum computing-based calculation of Dyson orbitals.
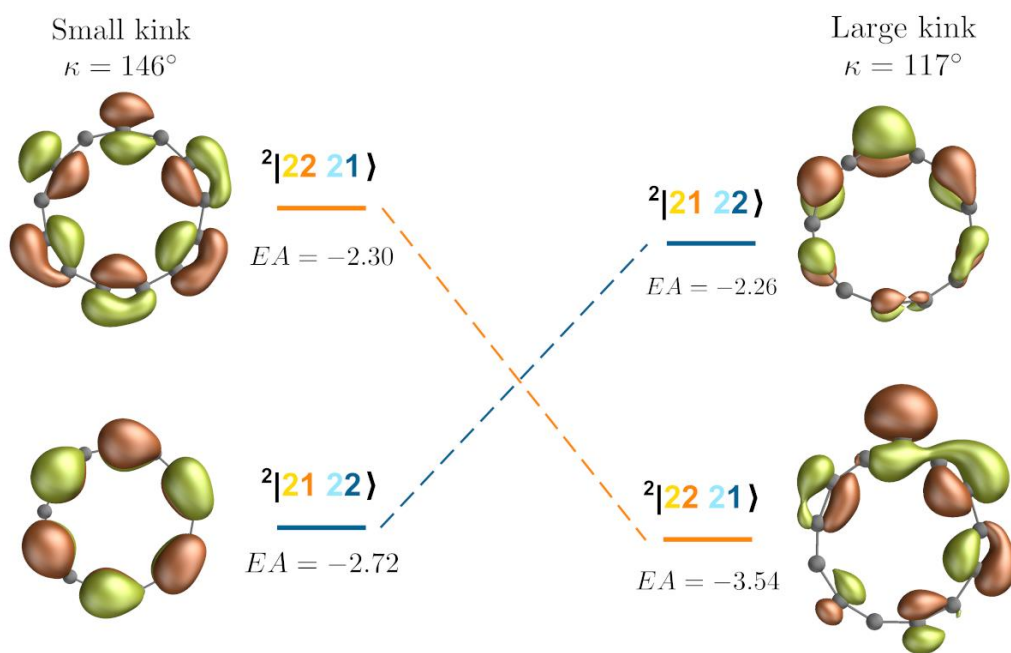

Figure S16. Dyson orbitals (at 0.05 a.u.) and corresponding electron affinities (*EA*) for electron attachment calculated with qUCCSD based on the cc-pVTZ basis set and an active space including 6 electrons and 4 orbitals. Dyson orbitals were calculated both for the "small kink" geometry, corresponding to the triplet equilibrium geometry (left part of the figure), and for the "large kink" geometry, corresponding to the closed-shell singlet equilibrium geometry (right part of the figure). Electron affinities (*EA*) in eV.

Explicitly correlated coupled clusters with singles, doubles and perturbative iterative triples (*48*) were done using the domain based local pair-natural orbital framework, F12-DLPNO-CCSD(T*). The calculations utilized the explicitly correlated cc-pVDZ-F12 basis, which gives results comparable to a 2-3 tier larger noncorrelated basis (*49, 50*). Single-point energies for two gas-phase geometries of C_{13} in the lowest singlet and triplet state are shown in fig. S17, but we note that the large values of the T_1 diagnostic make these results somewhat unreliable. These calculations were done using ORCA (*51*).
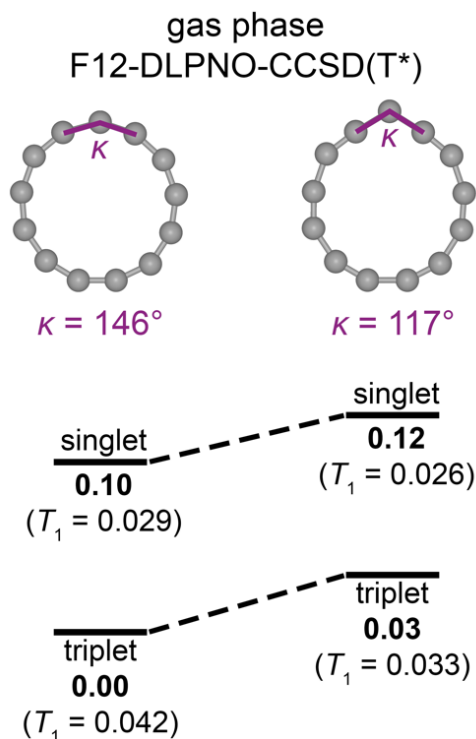
Figure S17. Relative energies (bold, in eV) of C_{13} in its singlet and triplet ground state, calculated using F12-DPLNO-CCSD(T*)/F12-cc-pVDZ at gas phase optimized geometries. The T_1 diagnostic values, which give a measure of multireference nature, are given in parentheses.

## 7. Additional experimental data on C$_{26}$
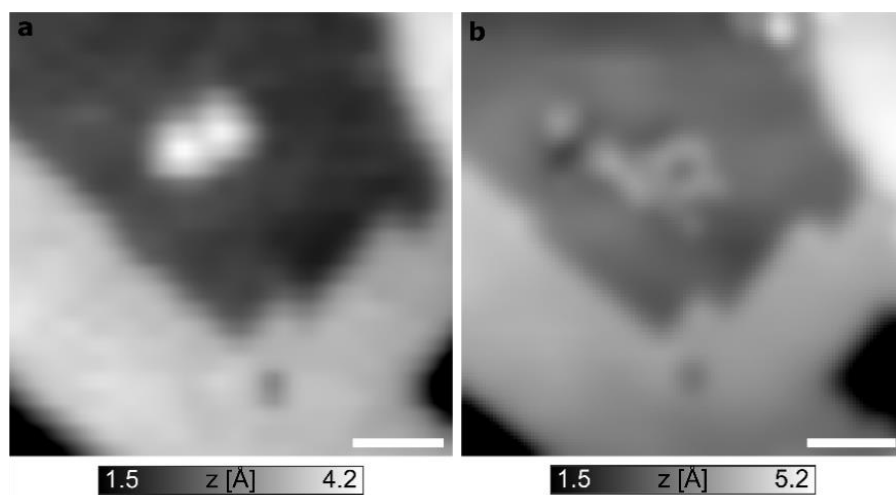
Figure S18. **Cyclo[26]carbon generation.** STM images ($V = 0.1$ V, $I = 0.5$ pA) of (**a**) two adjacently adsorbed precursor molecules and (**b**) same sample area after applying a voltage pulse of $V = 4.3$ V, in this case at a constant current of $I = 1.0$ pA, resulting in the formation of cyclo[26]carbon, C$_{26}$ (**b**). (**a**) recorded with a metallic tip, (**b**) recorded with a CO-functionalized tip. AFM data and STM orbital density maps of the C$_{26}$ molecule imaged in (b) are shown in the main text in Fig. 4. Scale bars 20 Å.
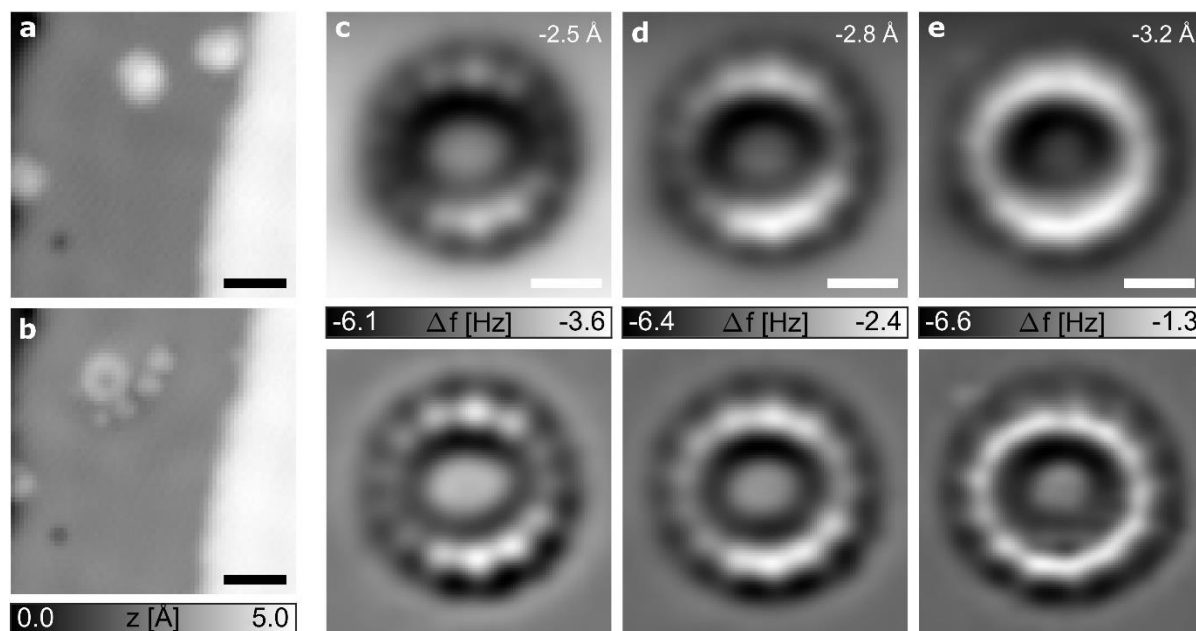
Figure S19. **Additional (high-resolution AFM) data on Cyclo[26]carbon.** STM images ($V = 0.2$ V, $I = 0.3$ pA) before (**a**) and after (**b**) applying a voltage pulse of $V = 4.4$ V to form the cyclo[26]carbon shown in this figure, from two adjacently adsorbed precursor molecules. (**c-e**) AFM images recorded at Δz

indicated in each panel with respect to a setpoint of $I = 0.3$ pA and $V = 0.2$ V; lower panels show Laplace-filtered data. Scale bars 20 Å in (a, b), 5 Å in (c-e).
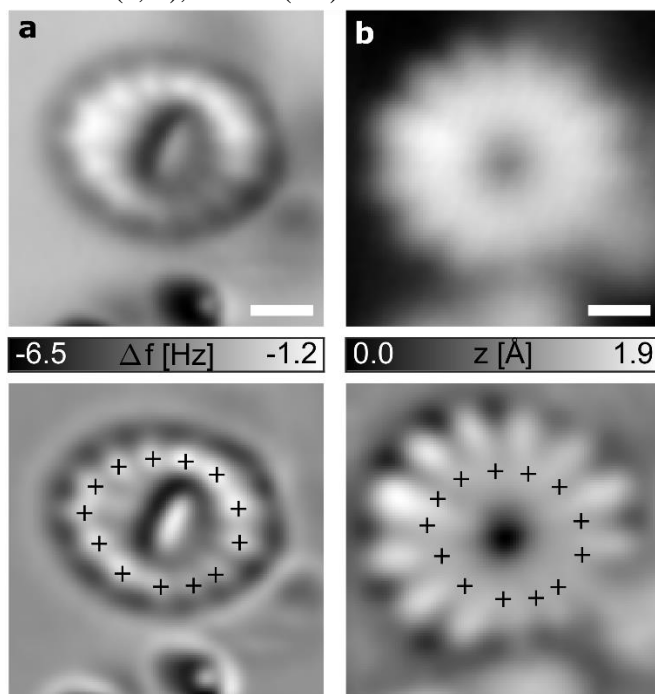
Figure S20. Additional (AFM and STM) data on Cyclo[26]carbon. (a) AFM ($\Delta z = -1.5$ Å with respect to a setpoint of $I = 0.3$ pA and $V = 0.2$ V). **(b)** STM data at the NIR ($V = 1.5$ V, $I = 0.3$ pA). The lower panels show Laplace filtered data. As for the cyclo[26]carbon shown in Fig. 4 of the main text, the 13 lobes of high density of the NIR are located above the long bonds of C_{26}, i.e., between the marks assigning the short bonds by the corresponding AFM image. We relate the asymmetry in the AFM image (a) to an asymmetric CO tip. The molecule is the same C_{26} as imaged in fig. S19, imaged with a different tip and at a different adsorption site. Scale bars 5 Å.
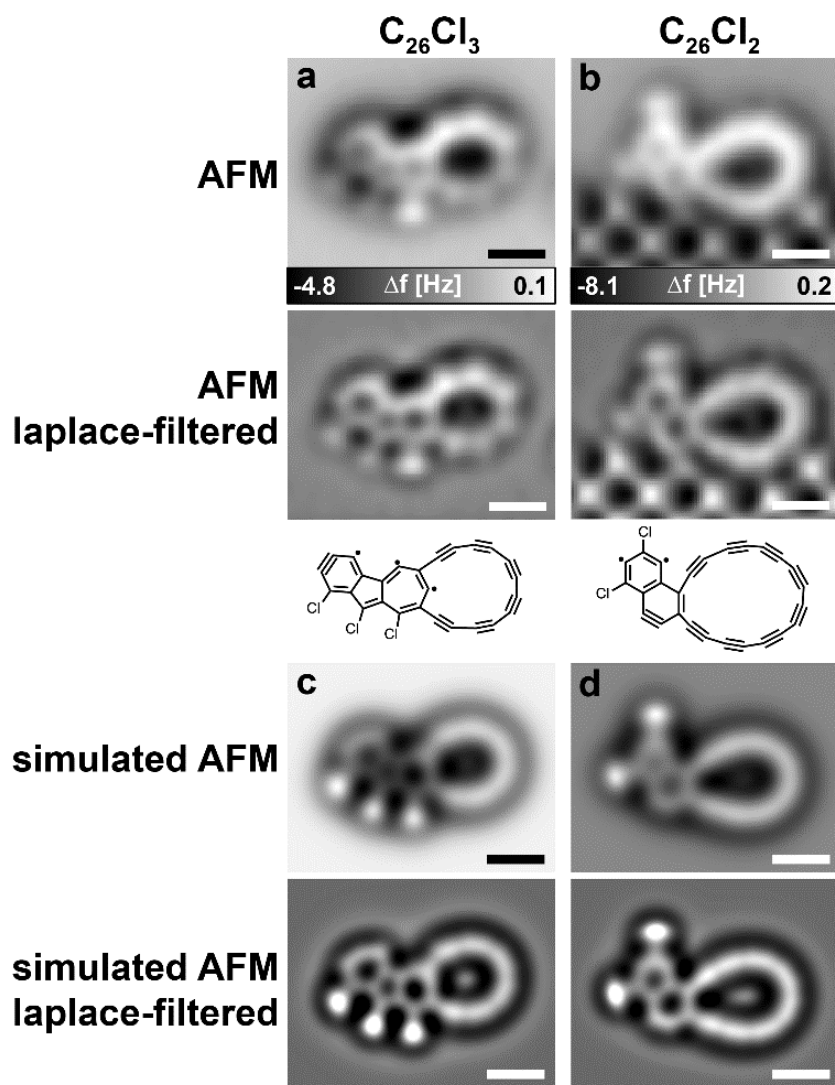
Figure S21. **Partly dehalogenated dimers generated by on-surface synthesis.** (**a, b**) AFM data (top), corresponding Laplace-filtered data (middle) and tentatively assigned Kekule structures (bottom). After a first voltage pulse of $V = 4.5$ V above two precursor molecules in close proximity on bilayer NaCl, the molecule in (a) was observed on bilayer NaCl. Applying another voltage pulse above the molecule in (a) resulted in the molecule shown in (b) and a change of its adsorption site. The molecule moved to monolayer NaCl where it is adsorbed next to a bilayer NaCl step edge, that is imaged in the bottom part of (b). (**c, d**) Simulated AFM images of proposed structures and corresponding Laplace-filtered images. Simulations of AFM images were performed based on DFT calculated xyz geometries using the Probe-Particle Model (*33*) using default CO-tip parameters (stiffness $k_x = k_y = 0.25$ N/m, $k_R = 30$ N/m), at an oscillation amplitude of $A = 0.5$ Å and a tip distance from the highest atom of 6.8 Å (c) and 6.7 Å (d). Scale bars 5 Å.